Triton's Variable Interaction With Neptune's Magnetospheric Plasma

Lucas Liuzzo[1] , **Carol Paty[2]** , **Corey Cochrane[3]** , **Tom Nordheim[3]** , **Adrienn Luspay-Kuti[4]**, **Julie Castillo-Rogez[3]**, **Kathleen Mandt[4]**, **Karl L. Mitchell[3]**, **Mats Holmström[5]** , **Peter Addison[6]** , **Sven Simon[6]** , **Andrew R. Poppe[1]** , **Steven D. Vance[3]** , and **Louise Prockter[4]**

[1]Space Sciences Laboratory, University of California, Berkeley, CA, USA, [2]Department of Earth Sciences, University of Oregon, Eugene, OR, USA, [3]Jet Propulsion Laboratory, California Institute of Technology, Pasadena, CA, USA, [4]Applied Physics Laboratory, Johns Hopkins University, Laurel, MD, USA, [5]Swedish Institute of Space Physics, Kiruna, Sweden, [6]School of Earth and Atmospheric Sciences, Georgia Institute of Technology, Atlanta, GA, USA

Abstract The tilt between Neptune's magnetic and rotational axes, along with Triton's orbital obliquity, causes a strong time variability of the moon's local electromagnetic environment. To constrain Triton's interaction with the ambient magnetospheric plasma, we apply a hybrid (kinetic ions, fluid electrons) model including the moon's ionosphere and induced field. To represent the extremes in the changes to the local electromagnetic field over a synodic rotation, we consider two orientations between the ambient magnetic field and flow velocity. For each, we first investigate the (analytical) magnetic signatures associated with the superposition of Triton's induced field and the magnetospheric field in the absence of any plasma interaction effects. To constrain the effect of Triton's ionosphere on the currents, we model the interaction between the ionospheric and magnetospheric plasma in isolation from the moon's inductive response, before combining these effects to investigate the complex scenario of plasma interaction and induction. Finally, we explore the sensitivity of the plasma interaction to changes in the ambient plasma density and the strength of Triton's inductive response. Despite plasma interaction signatures that dominate the plasma perturbations far from the moon (beyond ∼3 Triton radii), we illustrate that the induced field is clearly discernible within ∼3 Triton radii, regardless of the moon's location within Neptune's magnetosphere. We find that the orientation of the magnetospheric field and velocity vectors strongly affects Triton's plasma interaction; at times, resembling those of Jupiter's or Saturn's moons, while at others, revealing unprecedented signatures that are likely unique to moons of the ice giants.

1. Introduction

Neptune's largest moon Triton (radius $R_T = 1,353$ km) is thought to be an erstwhile Kuiper belt object that was captured by the ice giant (Agnor & Hamilton, 2006). Orbiting at a radial distance of $14.4 R_N$ (radius of Neptune $R_N = 24,622$ km), Triton is always located within Neptune's magnetosphere (Curtis & Ness, 1986; Mejnertsen et al., 2016; Ness et al., 1989; Richardson, 1993). The moon's highly inclined orbit—tilted nearly 157° with respect to its parent planet's rotational equator—results in a retrograde orbital motion around Neptune. Triton possesses the second-most dense moon atmosphere in the solar system after Titan (Broadfoot et al., 1989; Strobel et al., 1990; Strobel & Zhu, 2017). Mainly comprised of neutral N_2, its maximum surface number density is on the order of 10^{15} cm^{-3}, with a scale height between 10 and 70 km (Broadfoot et al., 1989). Additionally, trace gases including methane are present, with surface densities below 10^{11} cm^{-3} (e.g., Summers & Strobel, 1991; Trafton, 1984; Krasnopolsky et al., 1992). This neutral envelope is predominantly ionized by a combination of magnetospheric electron impacts and photoionization, resulting in an ionospheric Pedersen conductance that may exceed 10^4 S (Strobel et al., 1990). In addition to this global atmosphere, observations during the Voyager 2 encounter of Neptune in 1989 indicated localized, geyser-like vapor plumes emanating from the surface to an altitude of ∼10 km (Smith et al., 1989). Since the moon's interior is likely differentiated in a hydrosphere and rocky mantle, it is possible that these plumes originate from a global, deep ocean sustained via radiogenic heating and/or tidal forcing (Nimmo & Spencer, 2015).

Measurements from the Voyager 2 encounter of Neptune indicate that this ice giant's dipole magnetic axis is tilted by 47° with respect to the planetary spin axis and is offset from the planet's center by $0.55 R_N$ (Connerney et al., 1991; Ness et al., 1989). This, combined with Triton's highly inclined orbit, causes the magnetospheric environment near the moon to continually vary in time, throughout its orbit, with the magnitude of the local field fluctuating from $3 \text{ nT} \leq |\mathbf{B}| \leq 12 \text{ nT}$ on timescales of Neptune's 14.4 h synodic period, as well as Triton's 141 h orbital period (Saur et al., 2010). Unlike near the Galilean moons of Jupiter, for example, all three components of Neptune's ambient magnetospheric field near Triton display strong variability, with each component at times comparable to the magnitude of the field itself (e.g., Ness et al., 1995). Hence, these variable magnetospheric conditions should generate induction currents within Triton's putative conducting subsurface ocean and its ionosphere, manifesting as an induced magnetic field outside of the moon, which can potentially be used to constrain their structure (Saur et al., 2010). Hence, the presence and detectability of such induction signatures may be key pieces of evidence in establishing whether Triton is indeed an ocean world—a body that hosts a deep surface liquid reservoir—that may be habitable, especially considering the rich chemistry observed near its surface (e.g., Cruikshank et al., 1984; Delitsky & Thompson, 1987; Ohno et al., 2021; Thompson & Sagan, 1990).

In addition to these local magnetic perturbations due to the presence of a potential induced magnetic field at Triton, the moon's local electromagnetic environment is also perturbed by currents that stem from Triton's interaction with the ambient Neptunian plasma. Due to the moon's retrograde orbit, this nearly corotating plasma (comprised of a nearly 2:1 ratio of hydrogen to nitrogen ions; see Summers & Strobel, 1991) continually overtakes the moon's orbital *leading* hemisphere at a relative velocity on the order of $|\mathbf{u}_0| \approx 40$ km/s (Strobel et al., 1990). Compared to the local Alfvén speed of approximately 200 km/s, the ambient flow around the moon is sub-Alfvénic with an Alfvénic Mach number of $M_A \approx 0.2$. Hence, as the magnetospheric field drapes around Triton's atmosphere, ionosphere, and any induced magnetic field, two Alfvén wings—a non-linear system of standing Alfvén waves—form and connect the moon to Neptune's ionosphere (see also Neubauer, 1980). Changes in the local magnetospheric field orientation during Triton's orbit cause a variability in the locations where these Alfvén wings connect to Triton.

The structure of Triton's Alfvén wings would be strongly affected by the presence of an induced field at the moon, causing their cross-sections to shrink compared to the case without any induced field at the moon (Neubauer, 1999). However, the plasma interaction in turn affects the structure of Triton's induced magnetic field, similar to the interaction at Jupiter's moons Europa or Callisto (see, e.g., Arnold et al., 2019; Blöcker et al., 2016; Harris et al., 2021; Schilling et al., 2008; Liuzzo et al., 2015): pileup of the local magnetic field compresses the induced field at the ramside hemisphere, while convection stretches it toward downstream. Despite this interaction, the Galileo spacecraft detected distinct signatures of the nearly unaltered induced fields at Callisto and Europa within a narrow region located near these moons' wakeside surfaces (Arnold, Liuzzo, & Simon, 2020; Addison et al., 2021; Liuzzo et al., 2016). It is therefore possible that a similar region where signatures of the "pure" inductive response, shielded from effects of the plasma interaction, also exists near Triton.

In addition to the ~14 and 141 h periodicities in the magnetospheric field near Triton, properties of the ambient plasma also vary over similar timescales (Decker & Cheng, 1994; Sittler & Hartle, 1996). This generates a time-variable plasma interaction that is dependent on changes in the upstream magnetospheric plasma conditions and may induce additional currents within the moon's ionosphere and potential ocean. Triton's various plasma interaction scenarios can be compared to, for example, the Galilean moons of Jupiter as they travel through the giant planet's magnetosphere (e.g., Arnold, Liuzzo, & Simon, 2020; Blöcker et al., 2016; Jia et al., 2008; Liuzzo et al., 2015, 2016; Paty & Winglee, 2004; Schilling et al., 2008). At Europa, Schilling et al. (2007) have shown that the variability in the resulting plasma interaction generates an additional inductive response that is less than 10% of the field induced by the periodicity of the magnetospheric field. This approach requires knowledge about the evolution of the ambient magnetospheric density over a full synodic rotation. However, no observations or models of Neptune's magnetosphere exist that constrain the time-variability of the ambient magnetospheric plasma at Triton's position. So, while the variability in currents associated with Triton's plasma interaction may contribute to the moon's inductive response, we do not include their effect here in this pilot study.

The electromagnetic field perturbations generated by the magnetospheric plasma interaction with Triton's atmosphere, ionosphere, and induced magnetic field remains unconstrained. The goal of this study is therefore to model this interaction to identify the degree to which plasma currents may potentially conceal the signature of a magnetic field induced within a subsurface ocean or ionosphere at Triton. In addition, by investigating the resulting plasma interaction for distinct orientations of the magnetospheric field with respect to the direction of impinging flow, we constrain the variability in this interaction as a function of Triton's position within Neptune's magnetosphere. This study is organized as follows: Section 2 presents a brief description of the model used to study Triton's plasma interaction, including our assumptions on properties of the moon's interior, atmosphere, and ambient magnetospheric environment. Results are provided in Section 3: first, we provide a systematic investigation of the signatures associated with Triton's inductive response in the absence of plasma interaction currents. Next, we provide a baseline that will allow isolating the impact of the plasma interaction on the ionosphere and induced field, by investigating the interaction between the magnetospheric plasma and Triton's atmosphere/ionosphere in the absence of any inductive response. Then, we constrain the combined scenario of plasma interaction *and* induction at the moon, for two representative locations of Triton within Neptune's magnetosphere. This section also includes a brief investigation into the sensitivity of the plasma interaction and induction signatures to the chosen assumptions. Finally, conclusions of our study and an outlook into the future of Triton science are provided in Section 4.

2. Methodology: The AIKEF Hybrid Model

Due to the weak magnetospheric field magnitude near Triton, the gyroradii of corotating magnetospheric ions (H^+ and N^+) range from $0.1–1.5 R_T$; the gyroradii of picked-up ionospheric (N_2^+) particles are even larger. Hence, a kinetic representation of ion dynamics near Triton is *required* to obtain an accurate picture of the electromagnetic fields resulting from, for example, asymmetries in ion pickup or the substantial velocity shear between magnetospheric and ionospheric plasma. In this study, we therefore apply the three-dimensional AIKEF hybrid model (Müller et al., 2011), which treats ions as individual macroparticles and electrons as a massless, charge-neutralizing fluid.

The hybrid approach is well-documented and has been used to investigate the plasma interactions of many solar system objects. Examples include Earth's Moon (e.g., Holmström et al., 2012; Liuzzo et al., 2021), the moons of Jupiter (e.g., Fatemi et al., 2016; Lipatov & Combi, 2006; Lipatov et al., 2010, 2013; Liuzzo et al., 2015, 2016; 2017, 2018; 2019a, 2019b; 2020; Lindkvist et al., 2015; Poppe et al., 2018; Sittler et al., 2013) and Saturn (e.g., Kriegel et al., 2009, 2011, 2014; Ledvina et al., 2012; Lipatov et al., 2012; Sillanpää et al., 2006; Sillanpää & Johnson, 2015), as well as Mercury (e.g., Exner et al., 2018; Kallio & Janhunen, 2003), Venus (e.g., Kallio et al., 2006; Martinecz et al., 2009), Mars (e.g., Kallio & Janhunen, 2001; Modolo et al., 2016), and Pluto (e.g., Barnes et al., 2019; Delamere, 2009; Feyerabend et al., 2017).

The AIKEF hybrid model has a long history of modeling the plasma interaction of various objects throughout the solar system, reaching quantitative agreement with spacecraft data acquired during multiple spacecraft encounters of these objects. For the Jovian moon Callisto, Liuzzo et al. (2015); Liuzzo et al. (2016) used AIKEF to study the plasma interaction with the moon's atmosphere and induced dipole from a potential subsurface ocean, and were able to disentangle plasma interaction currents from induction signatures in magnetometer data obtained during the Galileo C10 encounter. Liuzzo et al. (2017, 2018) then applied the model to identify regions near Callisto that are most likely to encompass induced fields that may be detectable during close flybys, and predicted the magnetic field signatures observable near the moon during the upcoming *JUpiter ICy moons Explorer* mission. At Europa, Arnold et al. (2019) used AIKEF to identify signatures of water vapor plumes in magnetic field data from the Galileo E26 flyby, while Arnold, Liuzzo, and Simon (2020) and Arnold, Simon, and Liuzzo (2020) provided a framework for the identification of plumes in magnetic field data and ion energy spectrograms from future flyby missions to this moon. AIKEF has also been used to describe the plasma environment of Pluto, matching data obtained during the New Horizons flyby (Feyerabend et al., 2017). This model has also been applied to study Earth's Moon (Liuzzo et al., 2021; Vernisse et al., 2013; Wiehle et al., 2011), investigating the lunar interaction for the distinct plasma environments the Moon experiences throughout its orbit, matching data from the ARTEMIS spacecraft. In addition, the three-dimensional electromagnetic field output from this model has been used to constrain
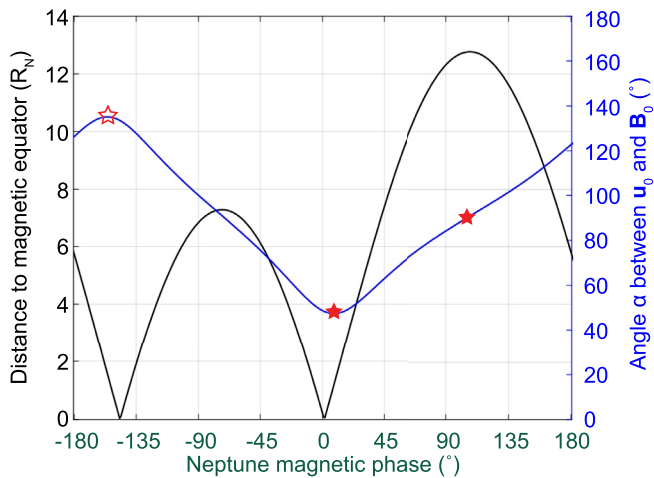
Figure 1. Variability in the ambient magnetic field near Triton's orbit over the course of a synodic rotation (magnetic phase) as obtained from the Connerney et al. (1991) model. Included are (blue) the angle α formed by the ambient plasma flow vector and the local magnetospheric field direction and (black) Triton's vertical distance to Neptune's magnetic equatorial plane. The two solid red stars illustrate the two orientations between $\mathbf{u}_0$ and $\mathbf{B}_0$ investigated in this study, at the minimum and an intermediate angle between these vectors. The scenario with a maximum angle between $\mathbf{u}_0$ and $\mathbf{B}_0$ (outlined red star) is *not* considered in this study, as the resulting signatures would be qualitatively similar to those for the minimum angle.

the energetic particle environments near the moons of Jupiter (Addison et al., 2021; Breer et al., 2019; Liuzzo et al., 2019a, 2019b, 2020) and Saturn (Kotova et al., 2015; Krupp et al., 2020; Regoli et al., 2016), reaching agreement with spacecraft measurements. The hybrid approach in general, and the AIKEF model in particular, is therefore well suited to study the plasma interaction of Triton. While we provide a brief discussion of the model inputs and assumptions below, further details on AIKEF can be found in any of the aforementioned publications.

2.1. Triton's Magnetospheric Plasma Environment

The combination of Triton's retrograde orbit around Neptune and the variability of the planetary magnetic field near the moon's orbit creates a highly dynamic local electromagnetic environment. To represent the magnetospheric field near Triton, we apply the Connerney et al. (1991) spherical harmonic magnetic field model, which constrains Neptune's tilted, offset magnetic field using data from the Voyager 2 encounter. Figure 1 displays this variability in the local field orientation with respect to the ambient plasma flow, along with the moon's distance to Neptune's magnetic equatorial plane, as determined from the model. Over the course of a full rotation, the magnitude of the ambient magnetospheric field oscillates between $3 \text{ nT} \leq |\mathbf{B}_0| \leq 12 \text{ nT}$ (see, e.g., Figure 10 of Saur et al., 2010), during which the angle α formed between the ambient plasma flow and the local magnetic field oscillates between approximately $47° < \alpha < 133°$. Figure 1 illustrates how Triton's location with respect to Neptune's magnetic equatorial plane is also highly variable: sometimes embedded within the magnetic equator, while at others located more than $12 R_N$ away from it. As shown by Mejnertsen et al. (2016) and consistent with the limited Voyager 2 data from within the Neptunian system, the plasma density decreases with increasing distance to the planet's magnetic equator (and thus, with angle α between $\mathbf{u}_0$ and $\mathbf{B}_0$ as shown in Figure 1). Hence, as Triton crosses Neptune's magnetosphere at L-shells ranging from ~14 to beyond 40 (Richardson et al., 1990), the oscillation in the moon's distance to Neptune's central plasma sheet causes the ambient plasma number density n_0 to reach a maximum value on the order of 10^{-1} cm^{-3} and a minimum nearly three orders of magnitude lower (e.g., Belcher et al., 1989; Richardson & McNutt, 1990; Richardson, 1993; Strobel et al., 1990; Sittler & Hartle, 1996; Zhang et al., 1991). Triton therefore experiences a highly variable local magnetospheric plasma environment during its orbit around Neptune.

Since the variability of Neptune's magnetosphere occurs on timescales of hours (compared to plasma convection timescales past Triton on the order of minutes), we focus on two "snapshots" that represent Triton's magnetic environment for the minimum and intermediate angle formed between the magnetospheric background field and ambient flow velocity (denoted by the two solid red stars in Figure 1). By doing so, we constrain two representative scenarios of Triton's interaction with Neptune's magnetospheric plasma. The first scenario corresponds to $\mathbf{u}_0$ and $\mathbf{B}_0$ nearly perpendicular to one another, with an angle α between these two vectors of $\alpha = 89°$. This case is similar to the orientation of $\mathbf{u}_0$ and $\mathbf{B}_0$ at, for example, Jupiter's and Saturn's inner moons. The second scenario, however, represents a case where $\mathbf{u}_0$ and $\mathbf{B}_0$ are minimized, forming an oblique angle of $\alpha = 47°$ to one another. Note that the maximum angle between $\mathbf{u}_0$ and $\mathbf{B}_0$ (i.e., $\alpha = 133°$ as denoted by the outlined red star in Figure 1) would generate plasma signatures that are qualitatively similar to those for the case of $\alpha = 47°$ (see also, e.g., Addison et al., 2021; Simon & Motschmann, 2009). We therefore do not investigate the scenario with $\alpha = 133°$ here. Specifics of the ambient plasma and magnetic field environments for these cases, as well as the inputs used for the hybrid model, are provided in Table 1.

Consistent with Strobel et al. (1990), we set the ambient relative flow velocity with respect to Triton to $|\mathbf{u}_0| = 43 \text{ km/s}$ and the magnetospheric plasma number density to $n_0 = 0.11$ cm^{-3}. Because there is currently no model that provides the change in the magnetospheric number density over a synodic rotation with respect to Triton, we assume the same density value of $n_0 = 0.11$ cm^{-3} for the two angles α considered. To

Table 1
Plasma Properties of Triton's Local Magnetospheric Environment Used as Input Into the Hybrid Model

Parameter	$\alpha = 89°$	$\alpha = 47°$
Average magnetospheric ion mass m_0 (amu)	7.5	7.5
Ionospheric ion mass (amu)	28	28
Ion charge q (e)	+1	+1
Magnetospheric bulk velocity $\mathbf{u}_0$ (km/s)	[+43, 0, 0]	[+43, 0, 0]
Magnetospheric number density n_0 (cm^{-3})[a]	0.11	0.11
Magnetospheric ion temperature (eV)	65	65
Magnetospheric electron temperature (eV)	30	30
Magnetic field $\mathbf{B}_0$ (nT)	[−0.195, −7.94, −1.99]	[+3.50, −0.0178, −3.76]
$\|\mathbf{B}_0\|$ (nT)	8.19	5.14
Convective electric field $\mathbf{E}_0$ (mV/m)	[0, −0.0856, +0.341]	$[0, -0.162, +7.65 \cdot 10^{-4}]$
$\|\mathbf{E}_0\|$ (mV/m)	0.352	0.162
Induced magnetic moment $\mathbf{M}_0$ (10^{16} Am^2)[a,b]	[+0.242, +9.83, +2.47]	[−2.17, +0.011, +2.33]
$\|\mathbf{M}_0\|$ (10^{16} Am^2)	10.1	3.18
Alfvén velocity $\|\mathbf{v}_{A,0}\|$ (km/s)	197.4	123.3
Alfvénic Mach number $M_{A,0}$	0.218	0.349
Magnetosonic Mach number $M_{MS,0}$	0.211	0.309
Sonic Mach number $M_{S,0}$	0.870	0.832
Simulation domain (R_T)	$-10 \leq x, y, z \leq +10$	$-10 \leq x, y, z \leq +10$
Average magnetospheric ion gyroradius r_g (R_T)	0.30	0.48
Ionospheric ion gyroradius r_g (R_T)	1.12	1.80

Note. Vectors are given in the Triton Interaction System (see Section 2.4).

[a]Section 3.3 investigates the sensitivity of the plasma interaction signatures to changes in this parameter. [b]Simulations *without* Triton's induced field (i.e., for the plasma interaction with Triton's ionosphere alone) do not use any induced magnetic moment at the moon.

constrain the sensitivity of the resulting plasma interaction to this assumption, Section 3.3 briefly highlights the effect that reducing the density has on the electromagnetic field perturbations.

2.2. Triton's Induced Magnetic Field

The 14 h synodic period of Neptune and the 141 h orbital period of Triton drive electrical currents within conducting media (e.g., a possible briny ocean and ionosphere) at the moon. In turn, these currents induce a secondary magnetic field signature with strength and orientation dictated by the properties of the potential ocean and ionosphere. Hence, Neptune's magnetosphere presents ideal conditions to study magnetic induction at Triton.

While the existence of a long-lived internal dynamo at Triton is unknown, the moon is likely too small to still possess a liquid core, despite its mantle having been hot enough for a metallic core to differentiate following initial capture (e.g., McKinnon & Kirk, 2007). As a relevant analog to Triton in terms of physical properties, Europa does not show signs of a dynamo (e.g., Schilling et al., 2004), which Kimura et al. (2009) also attributed to rapid cooling due to a small rocky mantle.

The conductance of Triton's putative subsurface ocean is unconstrained; however, contributions of potential dissolved electrolytes to the ocean may come from the leaching of elements from the rock as a result of interaction with water and dissolution of accreted volatiles such as CO and CO_2 (leading to the production of carbonates), as well as NH_3 (leading to the production of ammonium). These species are expected to be abundant in Triton per its accretion in the Kuiper Belt (Shock & McKinnon, 1993). This mixture leads to

abundant Na^+, NH_4^+, and HCO_3^- in solution, on top of Cl^- (Marion et al., 2012). This chemistry has been found at the dwarf planet Ceres (Raponi et al., 2019). Soda lakes on Earth, which are also rich in Na^+ and HCO_3^-, have electrical conductivities of a few S/m for a salinity of a few wt.% and near 0° C (e.g., Jellison et al., 1999). In the case of Triton, a thick, global ocean ($\geq$200 km) is expected based on the moon's geologically young surface, likely sustained by obliquity-driven tidal heating (Nimmo & Spencer, 2015). The presence of a thick liquid layer, combined with an electrical conductivity that is $\geq$1 S/m (inclusive of margins), would lead to a conductance that is likely $\geq 2 \cdot 10^5$ S.

Similar to the hypothesized Triton ocean, the icy Galilean moons possess subsurface oceans with conductances on the order of 10^4 S, sustained by thermal contributions from accretional and radiogenic sources in addition to tidal heating—except for Callisto, which receives negligible tidal heat (see, e.g., Schilling et al., 2007; Seufert et al., 2011; Saur et al., 2015; Vance et al., 2021). Each of these moons displays strong inductive responses to the changing magnetic field of their ambient magnetospheric environments (e.g., Kivelson, 2000; Saur et al., 2010) which, outside of their conducting layers, are well-represented using a magnetic moment located at the center of each moon (e.g., Zimmer et al., 2000). For Triton, we therefore use a similar inductive response as observed at the Galilean moons.

Following the approach of Zimmer et al. (2000), we assume that the time-varying magnetospheric field is spatially uniform on the length scales of Triton's local plasma interaction, and assume a single, spherically symmetric conducting layer surrounding the moon. In this case, the magnetic field resulting from Triton's inductive response can be written as

$$\mathbf{B}_{ind} = \frac{\mu_0}{4\pi r^5} \left[3 \left(\mathbf{r} \cdot \mathbf{M}_0 \right) \mathbf{r} - r^2 \mathbf{M}_0 \right]. \tag{1}$$

Here, $\mathbf{r}$ represents the position outside of Triton, with the induced magnetic moment $\mathbf{M}_0$ written as

$$\mathbf{M}_0 = -\frac{2\pi}{\mu_0} A e^{i\phi} \mathbf{B}_0 R_T^3, \tag{2}$$

with (normalized) amplitude A and phase lag of the inductive response ϕ relative to the ambient field. In the absence of any additional currents from the plasma interaction, the total magnetic field observable outside of Triton's ionosphere is therefore given by the superposition of $\mathbf{B}_0$ and $\mathbf{B}_{ind}$. At Europa and Callisto, data from Galileo encounters suggest that the response to the changing magnetospheric field is nearly instantaneous, with any phase lag responsible for less than 10% of the total induced signal (i.e., $\phi \approx 0$; see, e.g., Zimmer et al., 2000). We therefore assume $\phi = 0$ for Triton's inductive response to Neptune's time-varying field.

Recently, Hartkorn and Saur (2017) showed that induction within Callisto's highly conducting ionosphere alone (i.e., *without* a subsurface ocean) may explain the magnetic field signatures observed during two of the Galileo encounters equally as well as induction within the moon's putative subsurface ocean. The Neptunian magnetospheric field near Triton's orbit displays a similar range of variability as the Jovian magnetospheric field near Callisto (cf. Connerney et al., 1991; Kivelson et al., 1999), and Triton's ionospheric conductance is approximately as large as Callisto's (cf. Strobel et al., 1990, 2002). Hence, it is reasonable to assume that Triton's ionosphere also possesses a substantial inductive response (although its amplitude and phase may be distinct from those of the ocean's response; see Cochrane et al., 2021). However, since the atmospheric scale height is below ~100 km, the ionospheric plasma is confined to a narrow region near Triton's surface (see also Liuzzo et al., 2015). Outside of this layer, the flow deflection around a dipole induced within a subsurface ocean would therefore appear similar to the pattern resulting from deflection around a dipole induced within the ionosphere, especially since the gyroradii of the magnetospheric ions well exceed the radial extent of this region with non-zero transverse conductivities (see Table 1). Hence, for the purpose of investigating the broad-scale signatures associated with Triton's plasma interaction, we treat these two regions as a single source of an induced field. This approach has been successfully used to reproduce Callisto's inductive response during multiple Galileo encounters (e.g., Liuzzo et al., 2015; 2016). For Triton, our initial results (i.e., for the values shown in Table 1) assume the normalized induced field amplitude has a value of $A = 0.5$. However, to represent the uncertainties in the induced fields generated within Triton's ionosphere, we also investigate the effect of setting the amplitude to $A = 1.3$ in Section 3.3. As demonstrated by Zimmer et al. (2000), this method allows us to investigate the effect of a stronger contribution to the inductive response from Triton's ionosphere on the plasma interaction signatures.

We note that the inductive response of Triton's subsurface and ionosphere have not been directly observed. Any non-spherical, global asymmetries in the conductance profile of a potential ocean would lead to a weak modification to Triton's dipolar inductive response compared to that assumed for this study (likely below 1% of the inducing field; see Styczinski & Harnett, 2021). Additionally, any non-uniformities within the ionosphere—especially including the day/night asymmetry associated with photoionization—likely lead to a non-dipolar inductive response, whose higher-order terms would be associated with strong uncertainties, since the exact structure of the ionosphere is poorly constrained. Regardless, we expect that the qualitative, large-scale plasma interaction features (i.e., the focus of this study) are robust against minor changes in these signatures. While we therefore consider only the dipolar component of an induced magnetic field at Triton, future targeted missions would be immensely beneficial for determining the effects of (potential) higher-order terms in the induced field on Triton's local environment.

2.3. Triton's Atmosphere and Ionosphere

To represent Triton's atmosphere within AIKEF, we apply the coupled Ion-Neutral-Photochemical (INP) model (de la Haye et al., 2008; Luspay-Kuti et al., 2015, 2016; Mandt et al., 2012). This model has been used to provide realistic, quantitative representations of the atmospheres of various solar system objects, including Titan and Pluto (e.g., Luspay-Kuti et al., 2017; Mandt et al., 2017), and is therefore highly suitable to generate a valid model of Triton's atmosphere. Including over 1,500 reactions between 50 neutral and 34 ion species, INP is a one-dimensional model that couples ion-neutral chemistry to solve the continuity equation throughout Triton's atmosphere and ionosphere. As sources to the atmosphere, INP includes photodissociation, bimolecular and termolecular chemistry, as well as electron recombination, while losses also include ion-molecule reactions as well as photoionization and electron impact ionization. While collisions and plasma slowdown may also affect generation of the atmosphere and ionosphere, considering their effect on the resulting profiles would require a sophisticated, two-way coupling between the INP and AIKEF models which is beyond the scope of this study.

Consistent with Voyager 2 measurements (e.g., Broadfoot et al., 1989; Strobel & Zhu, 2017), we set Triton's neutral surface number density to 10^{15} cm^{-3}. The altitude profile of the neutral density is then calculated by accounting for the vertical diffusion and photochemical production and loss of the atmosphere, with scale heights that are consistent with Voyager two observations (Broadfoot et al., 1989). To obtain the neutral profile in three dimensions, we assume that the atmosphere is spherically symmetric about the moon.

Triton's atmosphere is ionized via a combination of solar photoionization and electron impacts from Neptune's magnetosphere (e.g., Sittler & Hartle, 1996). To calculate the photoionized component of the neutral atmosphere profile, we apply the High-resolution Extreme UltraViolet irradiance model for Aeronomic Calculations (HEUVAC; Richards et al., 2006), which has previously been incorporated into AIKEF (Feyerabend et al., 2015, 2017; Liuzzo et al., 2015). As input into this model, we assume an F10.7 cm solar radio flux value of 160 SFU, consistent with the observed value at the time of the Voyager 2 encounter of Triton (Krasnopolsky et al., 1992). We apply photoionization cross-sections for the atmospheric species and calculate the resulting production rate throughout the atmosphere at a wavelength resolution of 0.01 nm (see also Luspay-Kuti et al., 2015). In addition, the interplanetary medium scatters Lyman-alpha photons, which affect the photochemisty of outer solar system objects; hence, we enhance the Lyman-alpha photon flux at Triton by a factor of 1.43, as suggested by observations at Pluto (e.g., Luspay-Kuti et al., 2017; Wong et al., 2017).

To calculate the contribution to Triton's ionosphere from electron impacts, we use PLANETOCOSMICS (Desorgher et al., 2005), a 3D Monte Carlo code that runs on the Geant4 framework (Agostinelli et al., 2003; Allison et al., 2006). This code has been utilized to study charged particle interactions at a number of planetary bodies, including Mercury (Gurtner et al., 2005, 2006), Venus (Dartnell et al., 2015; Nordheim et al., 2015), Earth (Usoskin et al., 2009), Mars (Gronoff et al., 2015), Europa (Nordheim et al., 2018, 2019), and Titan (Gronoff et al., 2009, 2011). For application to Triton, we use the optimized Livermore low energy electromagnetic model, whose ionization cross sections are based on the Evaluated Electron Data Library (e.g., Perkins et al., 1991). As input, we apply the ambient electron energy spectrum in Figure 9 of Sittler and Hartle (1996) for energies between 100 eV and 1 MeV, with a temperature of 300 eV and density of $3 \cdot 10^{-3}$ cm^{-3}. This spectrum represents the magnetospheric electron population as measured during the Voyager 2 encounter near Triton's minimum L-shell of ~14 by the Plasma Science Experiment and the

Low Energy Charged Particle Experiment. We use a power law to extrapolate this spectrum up to 10 MeV, consistent with the electron energies present within Neptune's magnetosphere (Krimigis et al., 1989; Mauk et al., 1991). Note that while Triton's perturbed electromagnetic environment likely affects the resulting electron precipitation and ionization patterns (e.g., Addison et al., 2021; Liuzzo et al., 2019a, 2019b, 2020; Regoli et al., 2016), we assume that electrons precipitate isotropically onto Triton's atmosphere as a first order approximation (see also Liuzzo et al., 2015).

The ion production profile from photoionization and electron impact ionization described above is input into AIKEF, where we assume that the resulting ionosphere consists entirely of molecular nitrogen, since that compound dominates Triton's atmospheric species by more than two orders of magnitude (e.g., Summers & Strobel, 1991; Trafton, 1984). The effect of trace species on the plasma interaction would therefore be minimal. Finally, we assume a temperature-dependent recombination rate within the AIKEF simulations (see also Arnold et al., 2019), which is an important loss process of Triton's ionospheric molecular nitrogen (e.g., Krasnopolsky & Cruikshank, 1995; Lellouch et al., 1992). The resulting ionospheric particles are introduced within the model using the approach described in Kriegel et al. (2011).

2.4. Coordinate Systems

For studying Triton, NASA's Navigation and Ancillary Information Facility (Acton, 1996) provides a Triton-centered coordinate system, "IAU_TRITON." In this system, $+z_I$ is aligned with Triton's spin axis, $+x_I$ points in the direction of Neptune, and $+y_I$ completes the right-handed, orthogonal system (nearly pointing along Triton's orbital direction). In the IAU_TRITON frame, the plasma velocity vector of the incident plasma $\mathbf{u}_I$ is given by

$$\mathbf{u}_I = \boldsymbol{\omega}_N \times \mathbf{p}_T + \mathbf{v}_T, \tag{3}$$

where $\boldsymbol{\omega}_N$ is Neptune's angular velocity (aligned with the planetary spin axis), $\mathbf{p}_T$ is the position vector of Triton with respect to Neptune, and $\mathbf{v}_T$ represents the retrograde orbital velocity of Triton (defined along $+y_I$).

Unlike for the "Moon-Phi-O" coordinate systems used at Jupiter (e.g., Kivelson et al., 2004) or the "Moon Interaction Systems" used at Saturn (e.g., Neubauer et al., 2006), the direction of the ambient plasma flow in IAU_TRITON is not fixed along any given axis, due to Triton's inclined orbit and the tilt of Neptune's magnetosphere. Hence, comparison of notable plasma interaction features between multiple positions of Triton within Neptune's magnetosphere is not straightforward in this system. To facilitate comparison between the cases in Table 1, we instead define a "Triton Interaction System" (henceforth referred to as "TRIST") in which the magnetospheric plasma flow direction is aligned with the $+x$ axis. In order to rotate the flow vector from IAU_TRITON ($\mathbf{u}_I = [u_{x,I}, u_{y,I}, u_{z,I}]$) into TRIST ($\mathbf{u} = [u_x, 0, 0]$), the rotation

$$\mathbf{u} = \boldsymbol{\mathcal{R}}_y \boldsymbol{\mathcal{R}}_z \mathbf{u}_I = [|\mathbf{u}_I|, 0, 0] \tag{4}$$

is performed. Here, $\boldsymbol{\mathcal{R}}_y$ is the matrix that rotates the orthogonal frame about the IAU_TRITON y_I axis and $\boldsymbol{\mathcal{R}}_z$ is the rotation matrix that rotates the orthogonal frame about the z_I axis, defined as

$$\boldsymbol{\mathcal{R}}_y = \begin{bmatrix} \cos\theta_{\mathbf{u}_I} & 0 & \sin\theta_{\mathbf{u}_I} \\ 0 & 1 & 0 \\ -\sin\theta_{\mathbf{u}_I} & 0 & \cos\theta_{\mathbf{u}_I} \end{bmatrix}$$

$$\boldsymbol{\mathcal{R}}_z = \begin{bmatrix} \cos\phi_{\mathbf{v}_I} & -\sin\phi_{\mathbf{v}_I} & 0 \\ \sin\phi_{\mathbf{v}_I} & \cos\phi_{\mathbf{v}_I} & 0 \\ 0 & 0 & 1 \end{bmatrix}. \tag{5}$$

In the above equation, $\theta_{\mathbf{u}_I}$ and $\phi_{\mathbf{u}_I}$ define the latitudinal and longitudinal angles, respectively, that relate the plasma velocity direction to the IAU_TRITON x_I axis, and are given by

$$\theta_{\mathbf{u}_I} = \arcsin\left(\frac{u_{z,I}}{|\mathbf{u}_I|}\right)$$

$$\phi_{\mathbf{u}_I} = -\mathrm{sign}\,(u_{y,I})\arccos\left(\frac{u_{z,I}}{|\mathbf{u}_I|\cos\theta_{\mathbf{u}_I}}\right). \tag{6}$$

Using the above, we are able to rotate the magnetospheric field vector from IAU_TRITON into TRIST. Figure 2 shows the orientation between the (blue) IAU_TRITON and (pink) TRIST systems for the two values of α considered in this study, along with a (yellow) magnetic field line that leaves Neptune and intersects the center of Triton as calculated by the Connerney et al. (1991) model.

Note that in TRIST coordinates, the inclination of Triton's orbit and the tilt of the Neptunian magnetosphere prevent the directions of the y and z axes from pointing toward the same direction for different orbital positions of Triton; i.e., the y axis does not always point toward Neptune and the z axis is in general *not* aligned with the planet's spin axis *nor* geographic North on Triton. As a result, it is not meaningful to compare the y and z components of any vector quantity between the different cases of α as described in Table 1 when using this system. For this reason, the discussion of our model results mainly focuses on the x component of the magnetic field and plasma flow velocity, which is *always* aligned with the direction of the ambient flow and is therefore comparable for two given positions of Triton within Neptune's magnetosphere.

3. Results

3.1. Influence of Triton's Induced Field on Its Local Environment

Before we can constrain the influence of Triton's interaction with the magnetospheric plasma on signatures associated with the moon's inductive response, we must first identify features of the induced magnetic field in the absence of any plasma interaction currents. Figure 3 displays the superposition of an induced field centered at Triton with the magnetospheric background field near the moon for two angles α between $\mathbf{B}_0$ and $\mathbf{u}_0$: (top row) $\alpha = 89°$ and (bottom row) $\alpha = 47°$. These cases are representative samples of the variability in the angle between the ambient flow and magnetospheric field vectors experienced by Triton during its excursion through Neptune's magnetosphere (also see the two solid red stars in Figure 1). Vectors for the background magnetospheric field ($\mathbf{B}_0$), the direction of the ambient flow velocity ($\mathbf{u}_0$), and the induced magnetic moment ($\mathbf{M}_0$) used for these cases (in TRIST coordinates) are given in Table 1. Since this figure does *not* include perturbations generated by Triton's interaction with the ambient Neptunian magnetospheric plasma, the field perturbations can be calculated analytically using Equations 1 and 2; use of the hybrid model is not be required in this case.

To facilitate comparison between the two cases, each panel in Figure 3 displays the perturbations of the magnetic field near Triton. Here, the perturbation of the magnetic field magnitude above or below the background value is defined as $\delta|\mathbf{B}| = |\mathbf{B}| - |\mathbf{B}_0|$, while the perturbation in the field component along the magnetospheric plasma flow direction is given by $\delta B_x = B_x - B_{0,x}$. Orange and red hues denote perturbations above the background value (i.e., $\delta|\mathbf{B}| > 0$ or $\delta B_x > 0$, respectively), while purple and blue hues correspond to perturbations below the background ($\delta|\mathbf{B}| < 0$ or $\delta B_x < 0$, respectively). Two different cutting planes are shown in Figure 3. The left two columns display field perturbations in the plane containing $\mathbf{B}_0$, $\mathbf{u}_0$, and the center of Triton. The angle α is included in these panels, measured against the $+x$ axis. The right two columns in the figure display the plane containing the ambient flow direction, the undisturbed convective electric field ($\mathbf{E}_0 = -\mathbf{u}_0 \times \mathbf{B}_0$), and the center of the moon. Note that neither of the cutting planes in Figure 3 coincides with any plane of TRIST.

The first column of Figure 3 reveals that the superposition of Triton's induced field with the magnetospheric background field generates two distinct regions in $\delta|\mathbf{B}|$ for the two angles α, driven by the anti-alignment between the induced magnetic moment $\mathbf{M}_0$ and $\mathbf{B}_0$. Near the "magnetic poles" of the induced magnetic moment (and where the magnetic field is nearly radial to the surface), the field magnitude is reduced since the magnetic moment is anti-aligned with the background field. Hence, for $\alpha = 89°$, the magnetic field has decreased nearly 2 nT below the background value of $|\mathbf{B}_0| \approx 8$ nT near the magnetic poles, while for $\alpha = 47°$, the field is reduced by ~1 nT below $|\mathbf{B}_0| \approx 5$ nT. Alternatively, near the "magnetic equator" of the induced
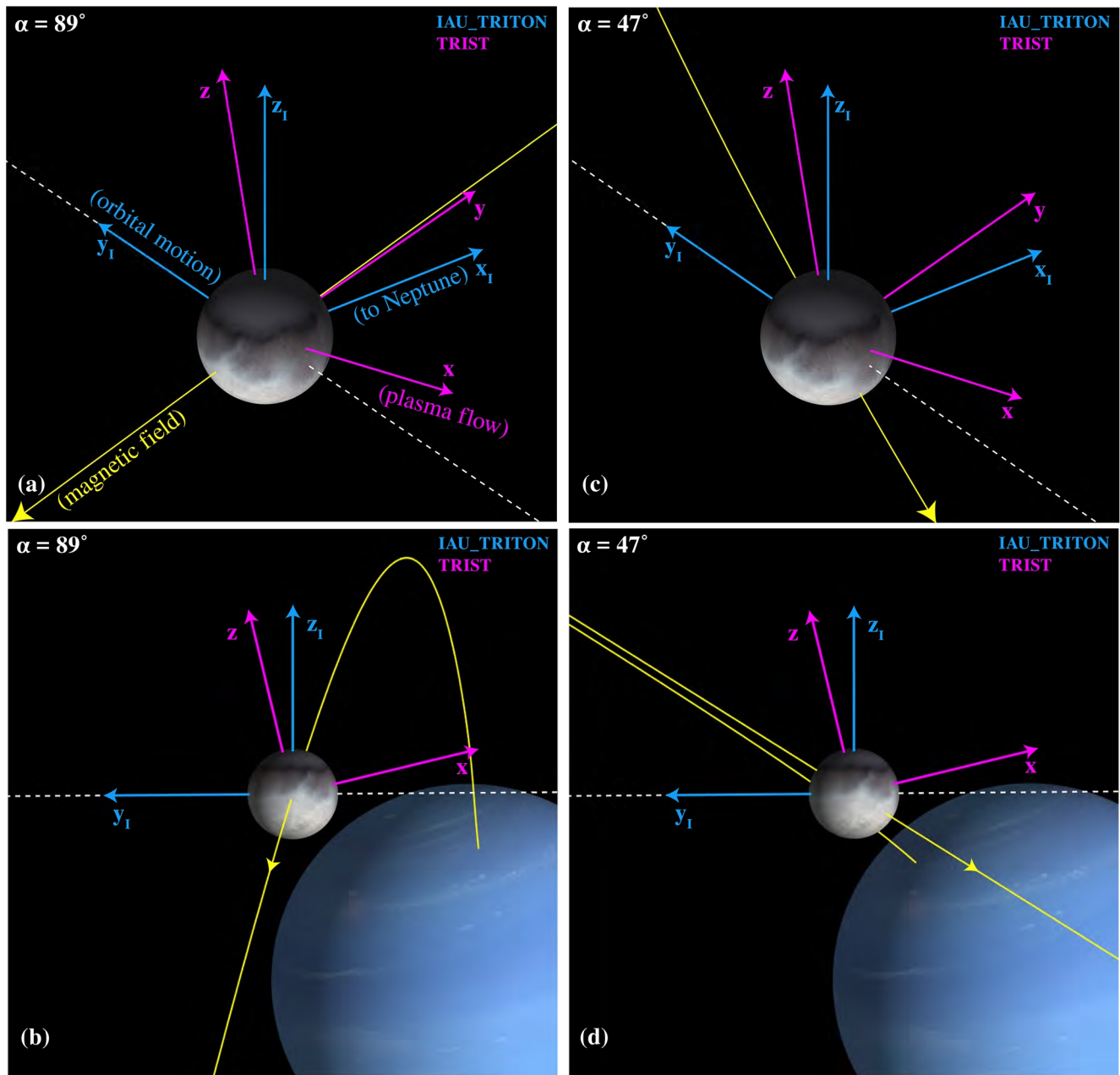
Figure 2. Coordinate system geometries used in this study. IAU_TRITON is shown in blue, in which $+x_I$ points toward Neptune, $+y_I$ is aligned with the direction of Triton's orbit, and $+z_I$ is along the moon's spin axis. The TRIST system is shown in pink, aligned so that the plasma flow direction is along the $+x$ axis. A magnetic field line connecting the center of Triton to Neptune as calculated by the Connerney et al. (1991) model is displayed in yellow. Panels (a) and (b) display the case of $\alpha = 89°$, whereas panels (c) and (d) display the orientation for $\alpha = 47°$. The dashed white line represents Triton's orbit.

field, where the field lines are more tangential to the moon, the magnitude is enhanced by a similar amount (~20%) for each case (orange hues). Since the magnitude of Triton's induced field is at most equal to the inducing field, there is no region of closed field lines near the moon (as occurs near Jupiter's moon Ganymede; see, e.g., Jia et al., 2008, 2009; Paty & Winglee, 2004; 2006). Hence, Triton's induced field is *not* strong enough to stand-off the ambient Neptunian field. Rather, the superposition of Triton's induced field with the Neptunian background field causes the magnetic field lines to be slightly "bulged" around the moon (see, e.g., Figure 3a), as also occurs near Europa and Callisto (e.g., Liuzzo et al., 2016; Zimmer et al., 2000). In the second column of Figure 3, the characteristic "shamrock leaves" of the induced field are visible
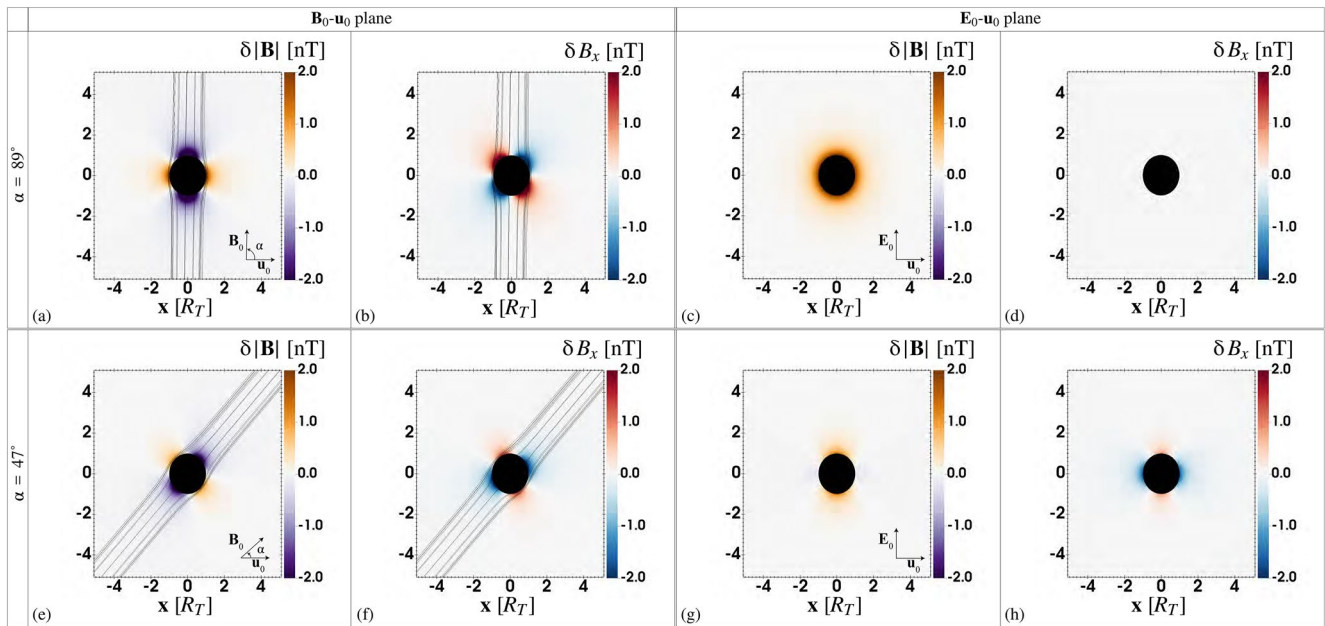
Figure 3. Superposition of the induced and background magnetic field near Triton *without* considering currents generated by the moon's plasma interaction. Perturbations over the background (i.e., $\delta|\mathbf{B}|$ and δB_x) are displayed. Orange and red hues denote perturbations above background, whereas purple and blue hues show perturbations below. The left two columns display quantities in the plane that cuts through the center of Triton and contains vectors $\mathbf{B}_0$ and $\mathbf{u}_0$; the right two columns display these quantities in the $\mathbf{E}_0$–$\mathbf{u}_0$ plane. The magnetic field is shown for two angles α between $\mathbf{B}_0$ and $\mathbf{u}_0$: (a–d) $\alpha = 89°$ and (e–h) $\alpha = 47°$. Vectors denote the direction of $\mathbf{u}_0$, $\mathbf{B}_0$, and $\mathbf{E}_0$. Magnetic field lines along a cylinder of radius $1.1 R_T$ centered at Triton are included in the $\mathbf{B}_0$–$\mathbf{u}_0$ plane. An amplitude of $A = 0.5$ (see Equation 2) is used.

near the moon in the flow-aligned component (i.e., B_x). These regions of alternating $\delta B_x > 0$ (red hues) and $\delta B_x < 0$ (blue hues) are most evident in the case of $\alpha = 89°$ [Figure 3b], but are still clearly visible with $\alpha = 47°$ [Figure 3f]. The right two columns in Figure 3 display the magnetic field perturbations near Triton in the $\mathbf{E}_0$–$\mathbf{u}_0$ plane. Compared to the case with $\alpha = 89°$, the convective electric field $\mathbf{E}_0$ is reduced by a factor of ~ 2 for $\alpha = 47°$ [vectors for $\mathbf{E}_0$ are included in Figures 3c and 3g].

3.2. Influence of Triton's Plasma Interaction on Its Local Environment

Having understood the magnetic signatures near Triton associated with an induced field in isolation from any plasma effects, we now investigate the influence of Triton's interaction with the Neptunian magnetospheric plasma on the induced field, ionosphere, and local plasma environment.

3.2.1. $\mathbf{B}_0$ Nearly Perpendicular to $\mathbf{u}_0$

Figure 4 displays perturbations in $|\mathbf{B}|$ and B_x near Triton when $\mathbf{B}_0$ and $\mathbf{u}_0$ are nearly perpendicular to one another ($\alpha = 89°$). The left column considers the interaction between Neptune's magnetospheric plasma and Triton's ionosphere *alone* (i.e., without any contribution from, or plasma interaction with, an induced field). The time-variability of Neptune's magnetospheric field likely generates an inductive response from the ionosphere. However, investigating the signatures associated with the interaction between Neptune's plasma and Triton's ionosphere *in isolation* from any induction effects—as displayed in the left column of Figure 4—allows us to establish a baseline to constrain the contribution of the induced field to the electromagnetic field perturbations. The center column in Figure 4 displays the plasma interaction with the ionosphere *and* induced field. To better illustrate changes in the resulting perturbations, the right column displays the differences between these two cases. The top six panels [Figures 4a–4f] display perturbations in the $\mathbf{u}_0$–$\mathbf{B}_0$ plane, whereas the lower panels [Figures 4g–4l] display perturbations in the $\mathbf{u}_0$–$\mathbf{E}_0$ plane.

Figure 4a highlights that Neptune's magnetic field piles up at Triton's ramside hemisphere $\sim 4R_T$ upstream of the moon and is enhanced above background by approximately 1 nT. In the wakeside hemisphere, an associated region forms where the magnetic field is reduced nearly 0.5 nT below background. As the magnetospheric field encounters Triton, it drapes around the ionosphere, generating perturbations in the flow-aligned component of the magnetic field [Figure 4d] forming Alfvén wings at large distances ($>\sim 4R_T$) to the moon. These perturbations reach values of $\delta B_x > \approx 1.5$ nT (i.e., nearly 20% of the background field magnitude). In the perpendicular plane containing $\mathbf{u}_0$ and $\mathbf{E}_0$ [see Figures 4g and 4j], the effect of the large gyroradii on the magnetic field are visible. Perturbations in the magnetic field are asymmetric in this plane, with the pileup region and associated wakeside cavity extending further along the direction of the ambient convective electric field.

The central column of Figure 4 shows the perturbations for the combined plasma interaction scenario with Triton's ionosphere *and* induced field. In the $\mathbf{u}_0$–$\mathbf{B}_0$ plane [Figures 4b and 4e], signatures of magnetospheric field line pileup and draping/Alfvén wings are visible, similar to the case with Triton's ionosphere alone. Closer to Triton's surface, however, the induced field dominates the magnetic perturbations: the magnetic field in this plane is reduced by more than 2 nT below the background value of $|\mathbf{B}_0| \approx 8$ nT near the "poles" of the magnetic moment, while the field is enhanced near its "equator" [see Figure 4b]. This enhancement within the pileup region in $|\mathbf{B}|$ is stronger than in the case without Triton's induced field [cf. Figure 4a]. Additionally in δB_x, the shamrock leaves of the dipole are still clearly visible near the surface [Figures 4e–4f]. While Triton's induced field is slightly compressed at its ramside and stretched into the wakeside hemisphere by the plasma interaction, the magnetic field perturbations within approximately $2R_T$ are only weakly influenced by plasma currents in this plane. Indeed, Figures 4c and 4f illustrate that close to Triton, the signatures in the $\mathbf{u}_0$–$\mathbf{B}_0$ plane are nearly indistinguishable from those of an induced field *in the absence* of plasma effects [cf. Figures 3a–3d].

Signatures of an induced field embedded within a draped magnetic field have also been observed near Jupiter's moons Callisto (Liuzzo et al., 2016) and Europa (Arnold, Liuzzo, & Simon, 2020; Addison et al., 2021). At Callisto, the orientation of the moon's induced field causes wakeside perturbations in the flow-aligned component of the magnetic field that are oppositely oriented from those associated with field line draping. Liuzzo et al. (2016) used this wakeside quasi-dipolar "core region" to identify the presence of Callisto's subsurface ocean during the Galileo C10 encounter, for which strong plasma interaction effects (i.e., signatures of field line draping and Alfvén wings) were present. Within Callisto's ramside hemisphere, however, the flow-aligned magnetic field perturbations generated by its induced field are of similar magnitude, and the same orientation, as those caused by field line draping (see figure 4b of Liuzzo et al., 2016). As discussed by Liuzzo et al. (2018), the magnetic signatures within this region generated by Callisto's plasma interaction and induced field appear similar along a one-dimensional spacecraft trajectory, complicating the identification of their source (i.e., induction vs. plasma interaction).

Figure 4e illustrates that this wakeside feature also occurs at Triton: for locations where field line draping generates $\delta B_x > 0$ [red in Figure 4e], the induced field causes $\delta B_x < 0$ [blue in Figure 4e], and vice versa [cf. Figure 4d]. However, unlike at Callisto or Europa, the signature of Triton's induced field is also clearly visible in the moon's *ramside* hemisphere (see also Figure 4f). The ram pressure of the upstream plasma near Triton is at least two orders of magnitude lower than near the Galilean moons ($n_0 m_0 u_0^2 \approx 10^{-3}$ nPa in this Triton simulation compared to 10^{-1} nPa at Callisto or 10 at Europa; see Kivelson et al., 2004; Liuzzo et al., 2016). Hence, the magnetic field perturbations associated with the draped field are weaker than those associated with the dipole, and signatures of the induced field are clearly visible within the moon's wakeside *and* ramside hemispheres.

At larger distances to the moon, comparison of Figure 4a and 4b, or Figure 4c and 4d, illustrate that the cross-sections of the Alfvén wings for the case with Triton's inductive response included are shrunk compared to the case without the induced field. As shown by Neubauer (1999), the maximum current flowing within an Alfvén wing is proportional to the radius of the wing tubes. However, the presence of an induced field reduces the cross-sections of the Alfvén wings, compared to the case without the induction effect. The currents along the wings—and hence the magnetic field perturbations—are therefore quenched by this induced field (see also Neubauer, 1999). Hence, the plasma interaction not only affects Triton's induced
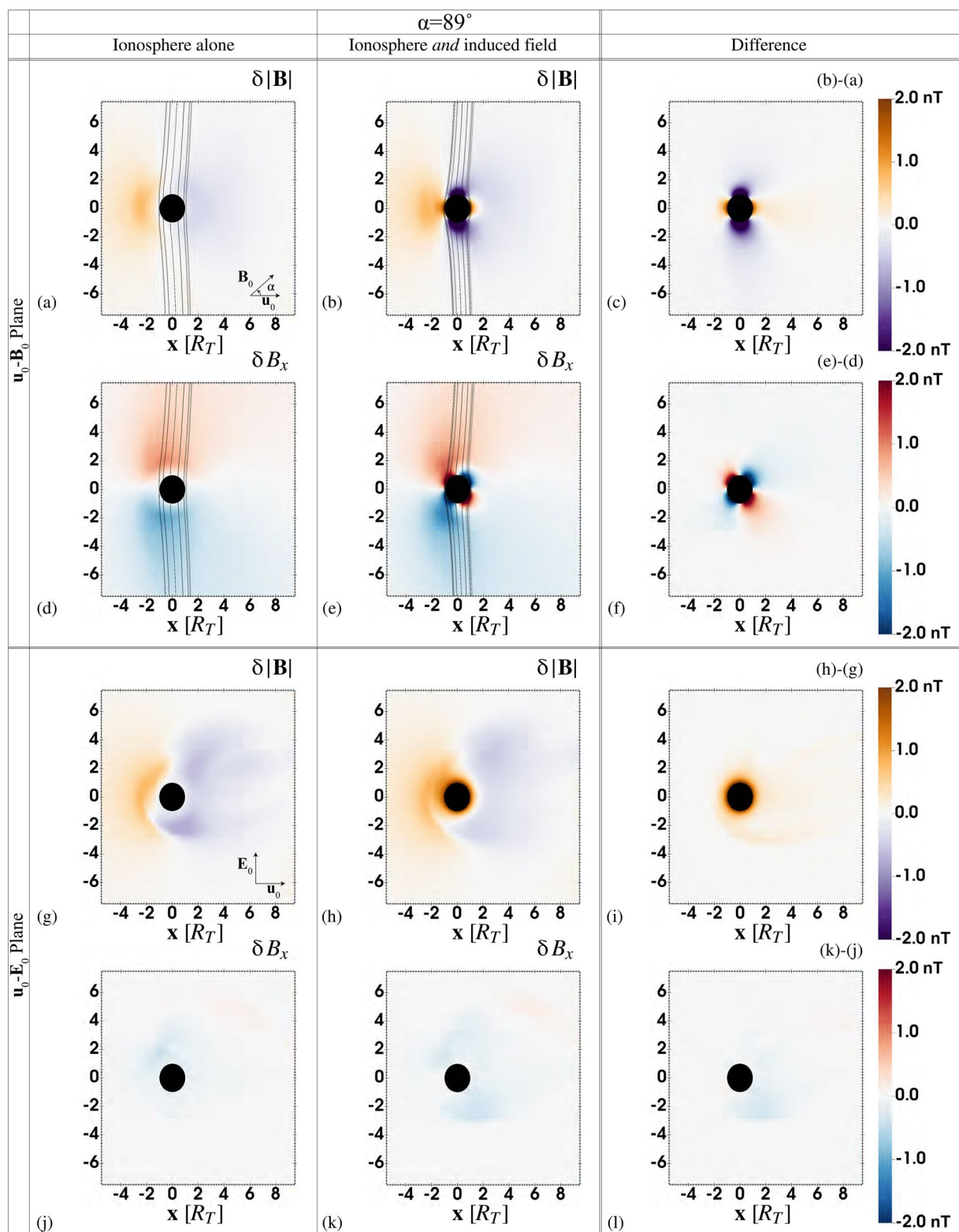
Figure 4.

field (e.g., by slightly compressing it at Triton's ramside), but conversely, the presence of the induced dipole affects features of the plasma interaction in the far-field.

In the $\mathbf{u}_0$–$\mathbf{E}_0$ plane, Figure 4h shows that even in the case of plasma interaction currents, the magnetic field is again dominated by the induced dipole within $\sim 2R_T$ of the moon (cf. Figure 3c). Farther from the surface, however, these features are again asymmetric in the direction (anti-)parallel to the convective electric field. These perturbations are similar to those arising from the interaction between the magnetospheric plasma and Triton's ionosphere alone. However, taking the difference between these two cases highlights that this wakeside cavity is nearly 1 nT weaker than in the case without Triton's induced field.

Figure 5 displays Triton's perturbed plasma environment for these two interaction scenarios (with Triton's ionosphere alone, and with the ionosphere and induced field) in the (left columns) $\mathbf{u}_0$–$\mathbf{B}_0$ and (right columns) $\mathbf{u}_0$–$\mathbf{E}_0$ planes. Figures 5a–5d display the ambient magnetospheric plasma density, whereas Figures 5e–h display the density of Triton's ionospheric population. For both scenarios (with and without the induced field), the magnetospheric particles are deflected around the draped field and exit the $\mathbf{u}_0$–$\mathbf{B}_0$ plane, slightly depleting the density downstream of the moon [Figures 5a–5b]. Figures 5c–5d illustrate that in the plane perpendicular to the magnetic field, this wake is slightly rotated into the direction of the convective electric field, approximately $\sim 5R_T$ wide and extending nearly $10R_T$ downstream.

Figures 5e–5h show that Triton's ionosphere dominates the ambient plasma density by orders of magnitude, reaching peak values near the surface of $\sim 10^4$ cm^{-3}. These particles mass-load the plasma, are picked up, and move toward downstream along cycloidal trajectories, thereby perturbing the local electromagnetic fields [see Figure 4]. The gyration of these ionospheric particles out of the $\mathbf{u}_0$–$\mathbf{B}_0$ plane causes the tail of ionospheric outflow to appear fragmented along the $+x$ axis in Figures 7e–7f. However, in the plane perpendicular to the magnetic field, Figures 5g–5h highlight that this is a result of the cycloidal motion of this pickup species. For both plasma interaction scenarios, large cycloidal arcs are visible along the direction of the electric field, as the gyration ($r_g > 1R_T$) and drift of these ionospheric particles carry them far from Triton in the direction of the corotation drift velocity. In addition, outflow of Triton's ionosphere forms a bifurcated tail reaching downstream densities of approximately 1–100 cm^{-3}, with a gap carved-out directly behind the moon where the density does not exceed ~ 0.01 cm^{-3}.

For this case of $\alpha = 89°$, signatures from Triton's plasma interaction resemble those at other icy moons throughout the solar system. A similar bifurcated, "filamented" tail structure visible in Figures 5g and 5h for Triton has been detected at Saturn's moon Titan during multiple flybys of the Cassini spacecraft (Coates et al., 2007; Modolo, Wahlund, et al., 2007; Modolo & Chanteur, 2008; Sittler et al., 2010; Feyerabend et al., 2015). However, we note that during those encounters, one segment of Titan's filamented tail was directed along the draped magnetic field (see Modolo, Chanteur, et al., 2007; Szego et al., 2007) in contrast to the orientation of the feature visible in Figures 5g and 5h). Another difference arises from the fact that, while its ambient plasma environment may at times be super- or sub-Alfvénic (potentially even changing during a single encounter; cf., e.g., Kallio et al., 2007; Sittler et al., 2010), Titan's Alfvén wing characteristics were mainly aligned with the ambient flow direction during those observations, which is unlike this case near Triton. Still, in addition to the similarities in these ionospheric outflow structures, the dense ionosphere of Triton, exposed to Neptune's variable magnetospheric environment, may also allow for the formation of "fossil" magnetic fields as have been observed at Titan (Neubauer et al., 2006; Bertucci et al., 2008; Simon et al., 2010). At Jupiter's moon Callisto, the ambient plasma environment is likewise highly variable (Kivelson et al., 2004). When located outside of Jupiter's magnetospheric current sheet, the sub-Alfvénic plasma generates strong signatures of field line pileup, draping, and Alfvén wings at Callisto (e.g., Liuzzo et al., 2015), similar to those displayed in Figure 4. Similar to Triton, outflow of Callisto's dense ionosphere is also highly asymmetric, with ionospheric gyroradii reaching up to 10 times the size of Callisto.

Figure 4. Perturbed magnetic field magnitude and flow-aligned field component near Triton for $\mathbf{u}_0$ nearly perpendicular to $\mathbf{B}_0$ (i.e., $\alpha = 89°$). The magnetospheric plasma interaction with (left column) the moon's ionosphere *alone* and (center column) the ionosphere *and* induced magnetic field are included, with the *difference* between these two scenarios (center column minus left column; see labels) displayed in the right column. Panels (a)–(f) display quantities in the plane cutting through the center of Triton and containing $\mathbf{B}_0$ and $\mathbf{u}_0$ [which flows along the $+x$ axis; see panel (a)], while panels (g)–(l) display the perpendicular plane, containing $\mathbf{u}_0$ and $\mathbf{E}_0$ [see panel (g)]. Results are shown at ~ 20 minutes after the simulation has been initialized with uniform upstream parameters. This corresponds to approximately four passages of the incident plasma flow through the simulation domain, and represents Triton's interaction after reaching a quasi-steady state.
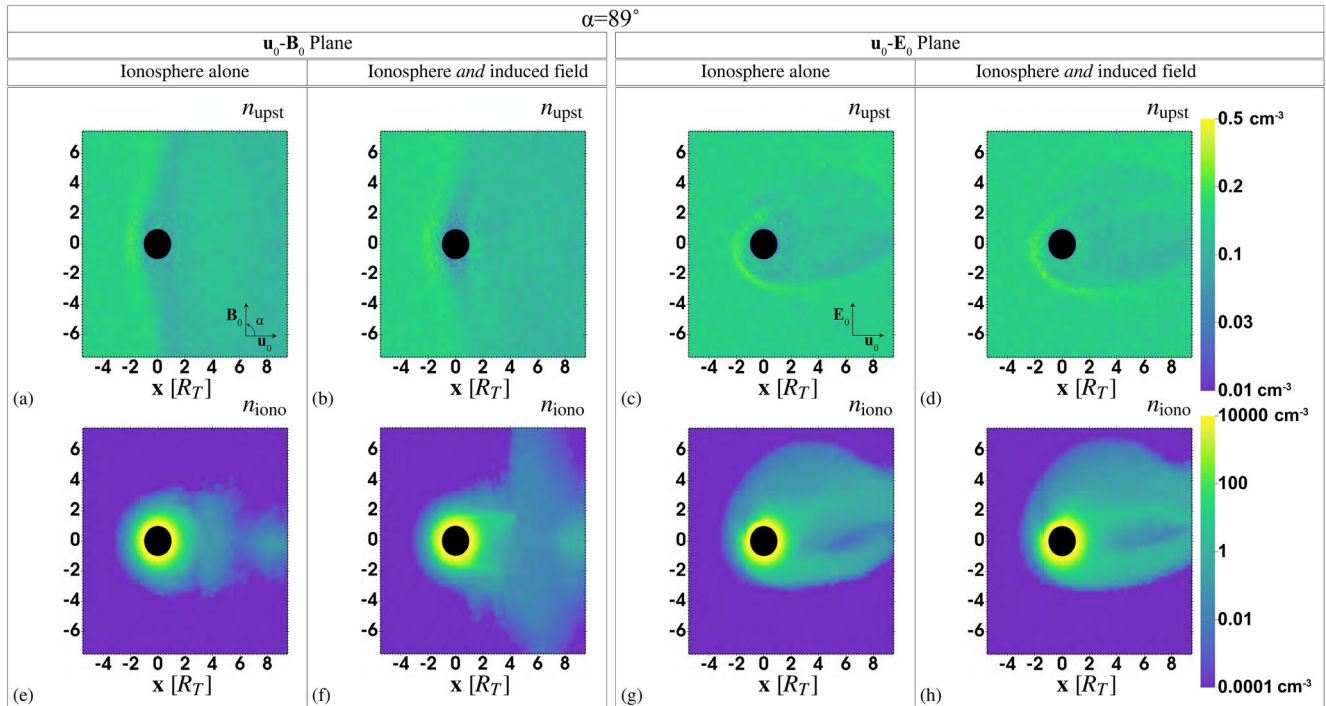
Figure 5. Plasma number densities near Triton for the case of $\alpha = 89°$. The (a–d) magnetospheric upstream and (e–h) ionospheric number densities in the (left columns) $\mathbf{u}_0$–$\mathbf{B}_0$ plane and (right columns) $\mathbf{u}_0$–$\mathbf{E}_0$ plane are included for the plasma interaction with Triton's ionosphere *alone* or the combination of Triton's ionosphere *and* induced field. Note the different color scales used for the two species.

3.2.2. $\mathbf{B}_0$ Oblique to $\mathbf{u}_0$

To investigate the effect of Triton's changing magnetic field environment on the resulting plasma interaction signatures, Figure 6 displays the magnetic perturbations in the $\mathbf{u}_0$–$\mathbf{B}_0$ and $\mathbf{u}_0$–$\mathbf{E}_0$ planes for an angle of $\alpha = 47°$ between $\mathbf{u}_0$ and $\mathbf{B}_0$. Compared to Figure 4, many features that were present with $\alpha = 89°$ are rotated in the plane containing $\mathbf{u}_0$ and $\mathbf{B}_0$, including the upstream enhancement of the magnetic field by ~20% compared to the background value and the associated wakeside magnetic cavity where the field is reduced by ~20% [Figures 6a and 6b]. Signatures of field line draping/Alfvén wings are also still visible in this plane, as displayed in Figures 6d and 6e, extending from the moon's ionosphere and induced field. The strength of these B_x perturbations within the region of draped field is slightly asymmetric about the x axis (see also Simon & Motschmann, 2009), and is reduced in magnitude by nearly a factor of two compared to the case of $\alpha = 89°$, reaching only $\delta B_x \approx 0.5$ nT = 10% of the background field value (compared to 1.5 nT ≈ 20% of the background field as seen in Figure 4). In the $\mathbf{u}_0$–$\mathbf{E}_0$ plane, features of Triton's plasma interaction—including the ramside pileup region and the associated, asymmetric wakeside magnetic cavity—are qualitatively similar to the case with $\alpha = 89°$, but again weaker by a factor of ~2 [cf. Figures 4g–4l].

Figure 6 also compares the case of the magnetospheric plasma interaction with and without Triton's induced field. Again, the right-hand column [Figures 6c, 6f, 6i, and 6l] illustrates that signatures of the induced field are clearly visible near the moon, with the magnetic field nearly dipolar within approximately $2R_T$ of the surface [cf. Figure 3]. Farther from the moon, plasma interaction signatures again dominate the magnetic field perturbations due to their r^{-1} decay with distance from the source (e.g., the Alfvén wings), compared to the r^{-3} decay of a dipole magnetic field. For each of these cases (with and without Triton's induced field included), a notable feature is present in the region downstream of Triton with respect to the ambient magnetospheric flow (i.e., the $x > 0$ half-space): tilted against the $+x$ axis by an angle of ~47°, a region of enhanced $\delta|\mathbf{B}| \approx 1$ nT extends away from the moon. In Figures 6a and 6b, this region is visible in orange within the bundle of magnetic field lines connected to Triton.
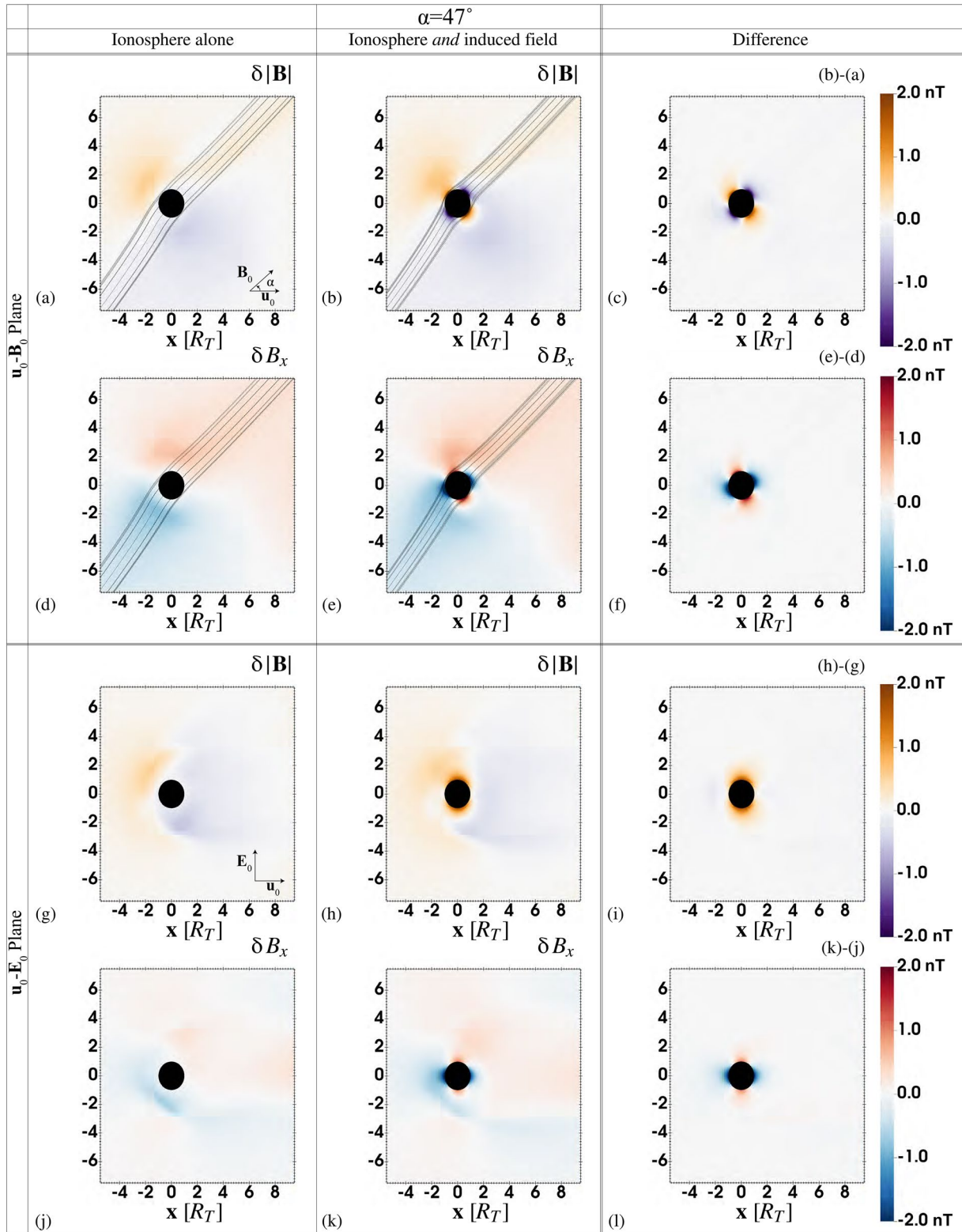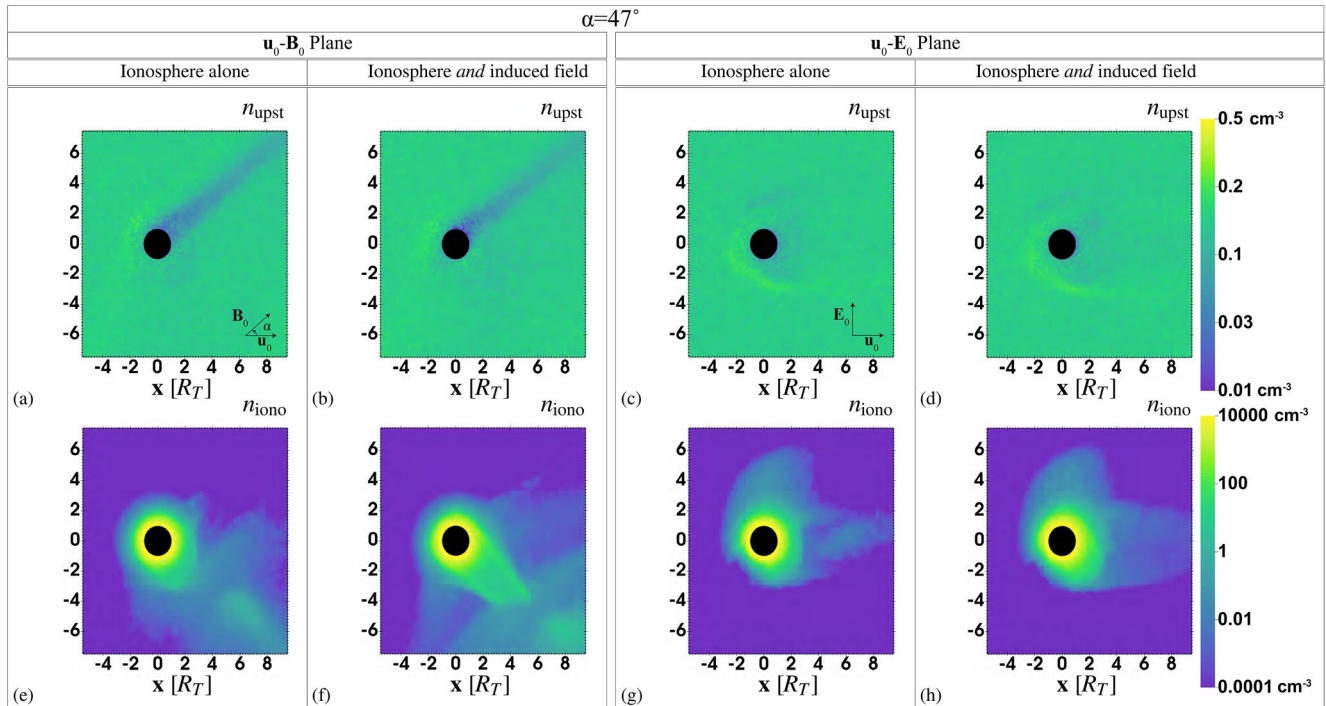
Figure 6. Perturbed magnetic field magnitude and flow-aligned component near Triton similar to Figure 4, but for the case of $\alpha = 47°$.

Figure 7. Plasma number densities near Triton as in Figure 5, but for the case of $\alpha = 47°$.

Figures 7a and 7b reveal the cause of these narrow enhancements in the magnetic field: a region of substantially reduced magnetospheric plasma density forms in Triton's downstream ($x > 0$) hemisphere in the $\mathbf{u}_0$–$\mathbf{B}_0$ plane for the cases with *and* without Triton's induced field. Note again, however, that these $\sim 2 R_T$-wide cavities are displaced out of the moon's geometric plasma shadow, tilted by $\sim 47°$. Within each of these tube-like regions, the magnetospheric plasma density is depleted by up to an order of magnitude compared to the background value.

To identify the generation mechanism of the tube-like plasma depletion tilted out of Triton's geometric plasma shadow, we must first present an analytical description of an Alfvén wing. Neubauer (1980) have shown that the Alfvén wing characteristics, defined as the superposition of the group velocity of the Alfvén wave (parallel/anti-parallel to the background magnetic field) with the bulk flow velocity in the ambient (i.e., undisturbed) plasma, are defined by

$$\mathcal{Z}_{0,\pm} = \mathbf{u}_0 \pm \frac{\mathbf{B}_0}{\sqrt{\mu_0 n_0 m_0}}.$$

(7)

Here, the upper sign corresponds to the propagation of Alfvén waves parallel to the magnetospheric background field, while the lower sign corresponds to wave propagation anti-parallel to $\mathbf{B}_0$. For simplicity, we will refer to these as the $\mathcal{Z}_+$ and $\mathcal{Z}_-$ Alfvén wings, respectively.

For $\mathbf{u}_0$ and $\mathbf{B}_0$ forming an angle of $\alpha = 47°$ and using the parameters in Table 1, the Alfvén wing characteristics are $\mathcal{Z}_{0,+} = [+127, -0.4, -90]$ km/s and $\mathcal{Z}_{0,-} = [-41, +0.4, +90]$ km/s (in TRIST as defined in Section 2.4). Hence, these characteristics point into opposite hemispheres with respect to the ambient flow direction: while one is oriented toward Triton's downstream hemisphere ($\mathcal{Z}_{0,+}$), the other points toward upstream ($\mathcal{Z}_{0,-}$). Additionally, for this case of $\mathbf{B}_0 \perp /\mathbf{u}_0$, the Alfvén characteristics are tilted at *different* angles against the background field direction (see also Neubauer, 1980): the angle formed between $\mathbf{B}_0$ and $\mathcal{Z}_{0,+}$ is 11.7°, while the angle between $\mathbf{B}_0$ and $\mathcal{Z}_{0,-}$ is 18.5°. Likewise, the Alfvén conductance (and hence, the strength of the magnetic field perturbations) are different between the two hemispheres (Neubauer, 1980). In contrast, for the scenario where $\mathbf{u}_0 \perp \mathbf{B}_0$ (i.e., where $\alpha \approx 90°$ as described in Section 3.2.1), the Alfvén wing character-

istics both point into Triton's wakeside hemisphere and are each tilted against the magnetospheric field by the same angle [see Figure 4].

Considering the incompressibility of the Alfvén wave far from Triton (i.e., beyond $\sim 3R_T$; see Figures 6a and 6b) and the constancy of the Elsässer variables $\mathcal{Z}_\pm$ along the Alfvén wing characteristics $\mathcal{Z}_{0,\pm}$, we find

$$\mathcal{Z}_\pm = \mathbf{u} \pm \frac{\mathbf{B}}{\sqrt{\mu_0 n_0 m_0}} = \mathbf{u}_0 \pm \frac{\mathbf{B}_0}{\sqrt{\mu_0 n_0 m_0}} = \mathcal{Z}_{0,\pm}. \tag{8}$$

Solving for the flow velocity $\mathbf{u}$ in the vicinity of the Alfvén wings (see also Simon, 2015; Simon et al., 2021) yields

$$\mathbf{u}_\pm = \mathbf{u}_0 \mp \frac{\mathbf{B} - \mathbf{B}_0}{\sqrt{\mu_0 n_0 m_0}} = \mathbf{u}_0 \mp \frac{\delta \mathbf{B}}{\sqrt{\mu_0 n_0 m_0}}. \tag{9}$$

Again, the upper sign corresponds to the $\mathcal{Z}_+$ wing while the lower sign corresponds to the $\mathcal{Z}_-$ wing. Hence, the magnetic field $\delta \mathbf{B}$ perturbed by the Alfvén wings can be applied to determine the plasma flow direction near the wings.

Figure 8 displays a three-dimensional view of Triton's perturbed electromagnetic environment as output from the hybrid model for the case of $\alpha = 47°$ (without the induced dipole included). The magnetospheric plasma density near the moon is displayed in the plane containing the magnetic field and ambient flow velocity vectors (as also shown in Figure 7a). Vectors denoting the magnetospheric bulk plasma flow direction in this plane are also included, with the direction of the ambient flow $\mathbf{u}_0$ aligned with the $+x$ axis. Magnetic field lines are shown in the Alfvénic far field (i.e., where $|\mathbf{B}| \approx |\mathbf{B}_0|$) and colored corresponding to the value of B_z such that blue hues denote perturbations below the background value ($B_{0,z} = -3.76$) while red hues show perturbations above background.

Figure 8 shows that along $\mathcal{Z}_+$ (within the $\mathcal{Z}_+$ Alfvén wing), B_z is enhanced to a value of $B_z \approx -3.5$ nT, resulting in a perturbation of $\delta B_z = B_z - B_{0,z} = +0.26$ nT. Along $\mathcal{Z}_-$, B_z drops below the background value to $B_z \approx -4.1$ nT, yielding $\delta B_z = -0.34$ nT. Using Equation 9, we see that the u_z component of the flow within the $\mathcal{Z}_+$ wing is therefore $u_{z,+} = -\frac{\delta B_z}{\sqrt{\mu_0 n_0 m_0}} \approx -6.3$ km/s; that is, along the $-z$-direction in TRIST coordinates (see also Figure 8) and away from Triton. However, within the $\mathcal{Z}_-$ wing, the flow $u_{z,-} = +\frac{\delta B_z}{\sqrt{\mu_0 n_0 m_0}} \approx -8.2$ km/s; that is, the magnetospheric plasma flow is directed *toward* Triton.

After the ambient magnetospheric plasma encounters the $\mathcal{Z}_-$ Alfvén wing far upstream of Triton, part of the flow is diverted around the wing and out of the plane containing $\mathbf{u}_0$ and $\mathbf{B}_0$. However, Equation 9 shows that a significant portion of the plasma is also deflected *along* the wing—in this case, anti-parallel to the $\mathcal{Z}_{0,-}$ characteristic—and *toward* Triton, as also demonstrated by the flow velocity vectors in Figure 8. As the magnetospheric plasma encounters the moon, it is partially absorbed, thereby generating a density depletion. Since the impinging plasma has been deflected by the $\mathcal{Z}_-$ Alfvén wing, this depletion does *not* form downstream of Triton with respect to the ambient plasma flow direction within the geometric plasma shadow. Indeed, the resulting tube-like density cavity is "displaced," tilted against the direction of the bulk plasma flow $\mathbf{u}_0$. Hence, the $\mathcal{Z}_-$ (i.e., upstream) Alfvén wing is responsible for diverting the ambient flow *toward* Triton *before it even encounters the moon* (in contrast to the $\mathcal{Z}_+$ wing, which deflects the flow away from the moon) and is subsequently absorbed, thereby generating a significant density cavity and plasma absorption signature.

This signature is unlike the plasma absorption signatures observed at any other solar system moon so far. At, for example, Saturn's moons Dione, Tethys, and Rhea (e.g., Khurana et al., 2017; Krupp et al., 2020; Roussos et al., 2008; Simon et al., 2009, 2011, 2012), or the terrestrial Moon (e.g., Fatemi et al., 2012; Halekas et al., 2005; Liuzzo et al., 2021; Poppe et al., 2014; Travnicek et al., 2005), cavities in the ambient plasma occur directly downstream with respect to the magnetospheric plasma flow direction. Yet, similar to these other moons, the decreased plasma density within Triton's tilted, tube-like density depletion also results in an enhanced magnetic field magnitude in order to maintain pressure balance (see Figures 6a and 6b).
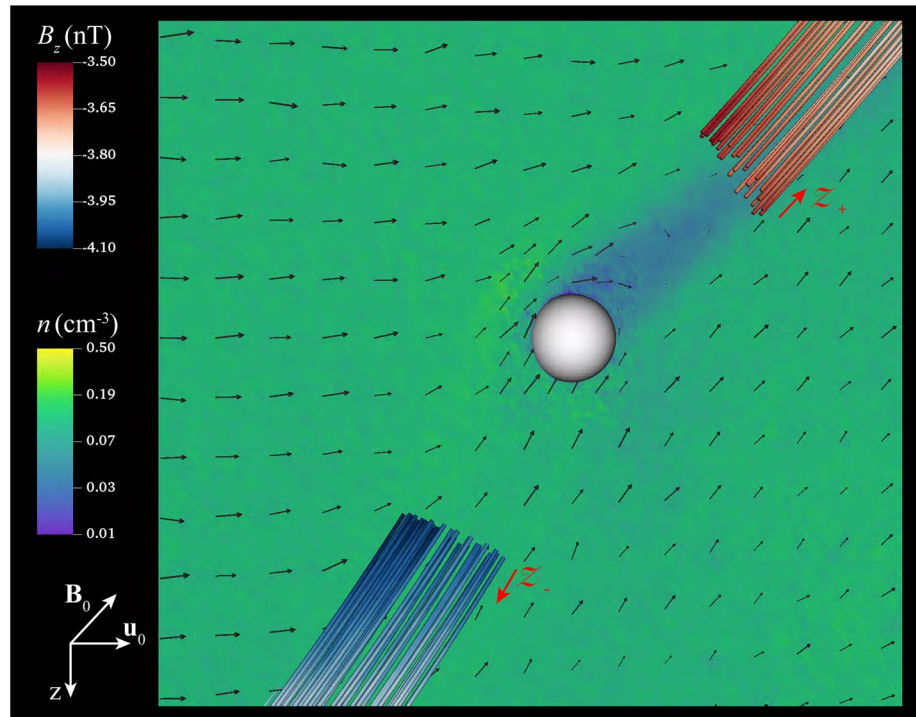
Figure 8. Triton's perturbed plasma environment for the case of $\alpha = 47°$ without the moon's induced field included. The magnetospheric plasma density near Triton is shown within the plane containing $\mathbf{u}_0$ and $\mathbf{B}_0$, as also displayed in Figure 7a. Vectors of the magnetospheric plasma flow velocity in this plane are also shown. Alfvén wings are included at larger distances from the moon in the Alfvénic far field, colored after the value of B_z in the simulation. The characteristics of the Alfvén wings are denoted by the red vectors.

At Triton, deflection of the ambient plasma flow by an Alfvén wing located upstream of the moon occurs due to the orientation of its parent planet's magnetosphere. However, this mechanism is not unique to Triton. Indeed, rearranging Equation 7, we see that the $\mathcal{Z}_{0,-}$ characteristic is located in the upstream hemisphere whenever

$$u_{0,x} < \left| \frac{B_{0,x}}{\sqrt{\mu_0 n_0 m_0}} \right|, \tag{10}$$

assuming here that the undisturbed plasma flows entirely along $+x$, as is the case in TRIST. Hence, the formation of such a displaced wake with respect to the ambient flow direction occurs whenever the group velocity of the Alfvén wave anti-parallel to the flow direction (i.e., $v_{A,0,x}$) exceeds the ambient flow speed. For the scenario described here with $\alpha = 47°$, the bulk velocity is a factor of ~2 below the component of the Alfvén velocity anti-parallel to the flow. Such an upstream Alfvén wing and the corresponding, displaced plasma absorption wake have never been observed by spacecraft so far. However, similar features also form as a result of the sub-Alfvénic interactions between stars and their exoplanets (Saur et al., 2013), and may be present at Uranus' moons as well considering this ice giant's magnetosphere is as highly dynamic as Neptune's (see, e.g., Cao & Paty, 2017, 2021; DiBraccio & Gershman, 2019). Future spacecraft encounters of Triton would therefore provide an opportunity to better investigate these plasma interaction features.

In the plane perpendicular to the magnetic field, Figures 7c and 7d illustrate that the magnetospheric plasma is asymmetrically diverted around the Triton obstacle anti-parallel to the direction of the ambient electric field, similar to the case with $\alpha = 89°$. For the ionospheric plasma, Figures 7e and 7f highlight that the direction of outflow is rotated along with the direction of the ambient magnetic field and consistent with the direction of $\mathbf{E}_0 \times \mathbf{B}_0$ (cf. Figure 5). Note that the ionospheric particles do *not* enter the displaced magnetospheric plasma cavity visible in Figures 7a, 7b, and 8. In the plane perpendicular to $\mathbf{B}_0$, signatures of ion gyration and outflow from Triton's ionosphere are present [see Figures 7g and 7h].
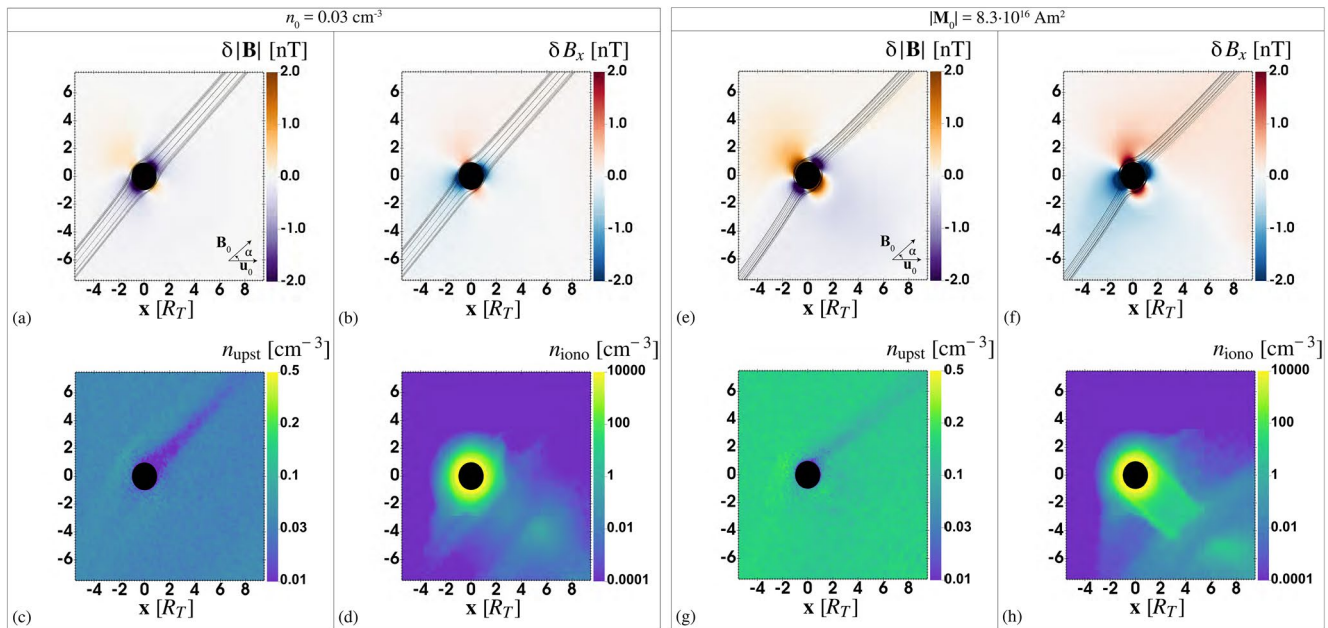
Figure 9. Sensitivity of Triton's plasma interaction to a (left columns; a–d) reduced ambient plasma number density to a value of $n_0 = 0.03$ cm^{-3} or (right columns; e–h) enhanced magnitude of the moon's induced dipole moment using an amplitude of $A = 1.3$. Quantities are displayed in the $\mathbf{u}_0$–$\mathbf{B}_0$ plane for an angle of $\alpha = 47°$ between the magnetospheric field and plasma bulk velocity vectors. Panels (a and b) and (e and f) display $\delta|\mathbf{B}|$ and δB_x, while panels (c and d) and (g–h) show the magnetospheric and ionospheric plasma number densities.

3.3. Sensitivity of Triton's Plasma Interaction to Differences in Its Magnetospheric Environment and Inductive Response

The previous sections provide an understanding of the interaction of Triton's ionosphere and induced field with the Neptunian plasma environment. Because Triton's magnetospheric environment is highly variable (on timescales much longer than the plasma interaction; see, e.g., Belcher et al., 1989; Zhang et al., 1991), and given the uncertainties in, e.g., the moon's internal structure or the conductance of its ionosphere, we now investigate the sensitivity of the plasma interaction to differences in Triton's local environment.

Figures 9a–9d displays results of the moon's plasma interaction using a reduced number density of the upstream plasma set to $n_0 = 0.03$ cm^{-3}, thereby reducing the Alfvénic and magnetosonic Mach numbers by a factor of ~2. As visible in Figures 9a and 9b, the most obvious feature in the magnetic field near the moon is Triton's induced field, with nearly dipolar signatures in $\delta|\mathbf{B}|$ and δB_x (cf. Figures 3e and 3f)). Similar to the case with a larger upstream density ($n_0 = 0.11$ cm^{-3}; see Section 3.2.2), currents from the plasma interaction again only weakly perturb the local magnetic field environment. Within the upstream pileup region, the magnetic field is enhanced less than 10% above the background value ($\delta|\mathbf{B}| \approx 0.5$ nT compared to $|\mathbf{B}_0| \approx 5$ nT).

To understand why Triton's interaction is so weak, we apply the approach in Saur et al. (2013) and focus on the $\mathcal{Z}_+$ Alfvén wing as an example. These authors define the strength of a moon's (sub-Alfvénic) interaction by the parameter

$$\varsigma = \frac{\Sigma_P}{\Sigma_P + 2\Sigma_A}, \tag{11}$$

where Σ_P denotes the ionospheric Pedersen conductance and the Alfvén conductance Σ_A is given by

$$\Sigma_A = \frac{1}{\mu_0 |\mathbf{v}_{A,0}| \sqrt{1 + M_A^2 + 2M_A \sin(90 - \alpha)}} \tag{12}$$

(see also Neubauer, 1980). The "interaction strength" ς is representative of how strongly the convective electric field (i.e., the bulk plasma velocity) is reduced within the Alfvén wing flux tube generated by an obstacle's interaction with its ambient plasma environment (Saur et al., 1999). A value of $\varsigma = 0$ denotes that no interaction occurs, while $\varsigma = 1$ signifies that the interaction is "saturated"; that is, that the plasma has been drained of its momentum and the resulting electromagnetic field perturbations near the obstacle are maximized. The value of ς is not only determined by parameters of a moon's ionosphere (i.e., Σ_P), but also by properties of its ambient plasma environment (e.g., n_0, $|\mathbf{B}_0|$, and $|\mathbf{u}_0|$). For this reason, an obstacle like Jupiter's moon Callisto—which possesses a dilute atmosphere but is exposed to only a weakly magnetized environment—can generate strong perturbations to its ambient electromagnetic environment with an interaction strength approaching $\varsigma \approx 1$ (e.g., Liuzzo et al., 2015). However, moons like Europa, Dione, or Rhea, which have dilute exospheres and are embedded within the strong magnetic environments of their parent planets' magnetospheres, only weakly perturb their local environment with $\varsigma \ll 1$ (see Saur et al., 2013).

Using an ionospheric Pedersen conductance for Triton of $\Sigma_P \approx 10^4$ S estimated by Strobel et al. (1990), we can calculate the interaction strength for the two cases of n_0 as considered in this study. For an ambient magnetospheric plasma density of $n_0 = 0.11$ cm^{-3} as discussed in Section 3.2.2, the Alfvén conductance is $\Sigma_A = 5$ S and the interaction strength reaches a value of $\varsigma = 0.9990$. In this case, the convective electric field already approaches zero and the electromagnetic field perturbations are nearly maximized. For the reduced density case of $n_0 = 0.03$ cm^{-3}, we find $\Sigma_A = 3$ S and the interaction strength becomes $\varsigma = 0.9994$. Because Triton's interaction is already nearly "saturated" for the case of $n_0 = 0.11$ cm^{-3}, reducing the ambient number density to $n_0 = 0.03$ cm^{-3} only causes small quantitative differences in the resulting electromagnetic field perturbations.

Figures 9c and 9d display the magnetospheric and ionospheric densities near Triton using $n_0 = 0.03$ cm^{-3}. In this case, the perturbed plasma environment is similar compared to the scenario with an enhanced ambient density. Figure 9c shows that a displaced cavity in the magnetospheric plasma again forms that is significantly tilted against the $+x$ axis due to flow deflection by the $\mathcal{Z}_-$ (upstream) Alfvén wing. In Figure 9d, the maximum ionospheric density still reaches values of nearly 10^4 cm^{-3} (see also Figure 7f).

Figures 9e–9h displays results from Triton's plasma interaction for a scenario in which the amplitude of the moon's inductive response is enhanced to $A = 1.3$ (see Equation 2), yielding a magnetic moment magnitude of $|\mathbf{M}_0| = 8.3 \cdot 10^{16}$ Am^2. To isolate the effect of the induced field on the plasma interaction signatures, the magnetospheric plasma density in this simulation is again assumed to be $n_0 = 0.11$ cm^{-3}. For this case with an enhanced inductive response representing a strong inductive signature from Triton's ionosphere, the magnetic field now remains quasi-dipolar within 3–4R_T of the surface in the upstream and downstream hemispheres. Notably in δB_x [Figure 9f], "shamrock leaves" of the induced field are now distinguishable, extending multiple radii from the moon. Compared to the case with a weaker inductive response ($A = 0.5$; see Section 3.2.2), the cross section of magnetic field lines extending from Triton are drastically reduced [cf. Figures 6b and 6e with Figures 9e and 9f] due to the enhanced magnitude of the induced magnetic moment (see also Neubauer, 1999). Other than the enhanced magnetic field perturbations, the remaining plasma quantities are similar for the case with a stronger (compared to a weaker) inductive response. The magnetospheric and ionospheric plasma densities in Figures 9g–9h display qualitatively similar features to the densities as shown in Figures 7b and 7f. Again, a region of depleted magnetospheric density forms at an angle against the ambient plasma flow direction displaced from the geometric plasma shadow, generated by flow deflection along the $\mathcal{Z}_-$ Alfvén wing *toward* Triton and its subsequent absorption. However, since the cross section of the $\mathcal{Z}_-$ wing is further reduced in this case with an enhanced inductive response, this displaced density depletion visible in Figure 9g is slightly weaker than in Figure 7b.

4. Discussion and Conclusions

In this study, we have modeled the interaction between Neptune's magnetospheric plasma and Triton's ionosphere and induced magnetic field. By investigating the contributions of Triton's ionosphere and induced field in isolation and in combination, we have identified regions near the moon where each of these competing effects generates dominant perturbations to the electromagnetic environment. To represent the periodic variability of the moon's ambient magnetospheric environment generated by Neptune's rotation

and Triton's orbital motion, we have investigated the resulting plasma interaction for two orientations and strengths of the magnetic field with respect to the ambient plasma flow velocity, and investigated the robustness in these signatures against the expected uncertainties in the upstream conditions and Triton's inductive response. A brief summary of our findings is as follows:

1. At times when the Neptune's magnetic field and magnetospheric flow velocity vectors are nearly perpendicular to one another, Triton's plasma interaction resembles those of various outer planet moons. The plasma interaction generates a magnetic field pileup region upstream of the moon, while field lines drape around the obstacle. The magnetospheric plasma environment displays signatures of flow deflection around the two Alfvén wings, while large ionospheric gyroradii generate asymmetries in the plasma outflow from Triton's ionosphere, resembling the environments of, for example, Callisto or Titan. Closer to Triton's surface (within $\sim$2–3R_T), the induced field dominates the magnetic field signatures in the wakeside *and* ramside hemispheres

2. At times when the magnetospheric field near Triton forms an oblique angle with the ambient flow velocity, Triton's resulting plasma interaction generates signatures that have never been observed at any other moon throughout the outer solar system. The characteristics of the two Alfvén wings are located in opposite hemispheres with respect to the impinging plasma flow (one upstream of the moon and the other downstream). The presence of an Alfvén wing upstream deflects a significant portion of the magnetospheric plasma flow along the wing and *toward* Triton. This plasma is then absorbed by the moon, forming a density depletion that is displaced out of Triton's downstream geometric plasma wake and tilted against the direction of the undisturbed magnetospheric flow. Besides the Neptunian system, the extreme obliquity and magnetic axial tilt of Uranus may also cause similar features to occur near this ice giant's moons as well. Such signatures also likely result from the plasma interactions of exoplanets with their parent stars. Hence, Neptune's magnetosphere serves as a unique laboratory to better understand these intra- and extra-solar system couplings

3. The magnitude of the magnetic field perturbations and the magnetospheric and ionospheric plasma signatures associated with Triton's plasma interaction are robust against changes in the ambient magnetospheric environment. Similarly, signatures associated with Triton's induced field remain detectable near the surface within the moon's ramside and wakeside hemispheres for a range of magnetospheric conditions, plasma interaction scenarios, and varying inductive responses of the moon

Our study has highlighted the impact that Triton's interaction with Neptune's magnetosphere has on the moon's local electromagnetic environment and on the potential detectability of induced magnetic fields. While future studies could refine some of the assumptions used in our model (e.g., by including atmospheric asymmetries and trace species, considering anisotropic magnetospheric electron precipitation, investigating the effect of induction within an ionosphere separately from that within an ocean, or by adding higher-order terms to Triton's inductive response), numerous unknowns regarding Triton's atmosphere, internal structure, and local magnetospheric environment still remain. Besides, since the Pedersen conductance of Triton's ionosphere exceeds the Alfvén conductance by four orders of magnitude, the moon's plasma interaction is already saturated with the maximum current flowing along the Alfvén wings (see also Neubauer, 1998).

While the Voyager 2 flyby provided a wealth of knowledge about Neptune and Triton, only future missions or comprehensive global modeling campaigns will be able to shed light on the mysteries of this ice giant system. In addition to answering outstanding questions about Triton, any future mission exploring the system may also have the opportunity to study plasma interaction signatures that have never before been observed, since the configuration and variability of Neptune's magnetosphere causes Triton's local plasma environment to be unique compared to those of other moons visited by spacecraft so far.

Data Availability Statement

Model products resulting from this study are available at doi.org/10.5281/zenodo.4917380.

References

Acton, C. H. (1996). Ancillary data services of NASA's navigation and ancillary information facility. *Planetary and Space Science*, *44*(1), 65–70. https://doi.org/10.1016/0032-0633(95)00107-7

Addison, P., Liuzzo, L., Arnold, H., & Simon, S. (2021). Influence of Europa's time-varying electromagnetic environment on magnetospheric ion precipitation and surface weathering. *Journal of Geophysical Research: Space Physics*, *126*, 1–42. https://doi.org/10.1029/2020ja029087

Agnor, C. B., & Hamilton, D. P. (2006). Neptune's capture of its moon Triton in a binary-planet gravitational encounter. *Nature*, *441*(7090), 192–194. https://doi.org/10.1038/nature04792

Agostinelli, S., Allison, J., Amako, K., Apostolakis, J., Araujo, H., Arce, P., et al. (2003). Geant4—A simulation toolkit. *Nuclear Instruments and Methods in Physics Research Section A: Accelerators, Spectrometers, Detectors and Associated Equipment*, *506*(3), 250–303. https://doi.org/10.1016/S0168-9002(03)01368-8

Allison, J., Amako, K., Apostolakis, J., Araujo, H., Arce Dubois, P., Asai, M., et al. (2006). Geant4 developments and applications. *IEEE Transactions on Nuclear Science*, *53*(1), 270–278. https://doi.org/10.1109/TNS.2006.869826

Arnold, H., Liuzzo, L., & Simon, S. (2019). Magnetic signatures of a plume at Europa during the Galileo E26 Flyby. *Geophysical Research Letters*, *46*(3), 1149–1157. https://doi.org/10.1029/2018GL081544

Arnold, H., Liuzzo, L., & Simon, S. (2020a). 1Plasma interaction signatures of plumes at Europa. *Journal of Geophysical Research: Space Physics*, *125*(1). https://doi.org/10.1029/2019JA027346

Arnold, H., Simon, S., & Liuzzo, L. (2020b). Applying ion energy spectrograms to search for plumes at Europa. *Journal of Geophysical Research: Space Physics*, *125*(9). https://doi.org/10.1029/2020JA028376

Barnes, N. P., Delamere, P. A., Strobel, D. F., Bagenal, F., McComas, D. J., Elliott, H. A., et al. (2019). Constraining the IMF at Pluto using new horizons SWAP data and hybrid simulations. *Journal of Geophysical Research: Space Physics*, *124*(3), 1568–1581. https://doi.org/10.1029/2018JA026083

Belcher, J. W., Bridge, H. S., Bagenal, F., Coppi, B., Divers, O., Eviatar, A., et al. (1989). Plasma observations near Neptune: Initial results from Voyager 2. *Science*, *246*(4936), 1478–1483. https://doi.org/10.1126/science.246.4936.1478

Bertucci, C., Achilleos, N., Dougherty, M. K., Modolo, R., Coates, A. J., Szego, K., et al. (2008). The magnetic memory of Titan's ionized atmosphere. *Science*, *321*(5895), 1475–1478. https://doi.org/10.1126/science.1159780

Blöcker, A., Saur, J., & Roth, L. (2016). Europa's plasma interaction with an inhomogeneous atmosphere: Development of Alfvén winglets within the Alfvén wings. *Journal of Geophysical Research: Space Physics*, *121*(10), 9794–9828. https://doi.org/10.1002/2016ja022479

Breer, B. R., Liuzzo, L., Arnold, H., Andersson, P. N., & Simon, S. (2019). Energetic ion dynamics in the perturbed electromagnetic fields near Europa. *Journal of Geophysical Research: Space Physics*, *124*(9), 7592–7613. https://doi.org/10.1029/2019JA027147

Broadfoot, A. A. L., Atreya, S. K., Bertaux, J. L., Blamont, J. E., Dessler, A. J., Forrester, W. T., et al. (1989). Ultraviolet spectrometer observations of Neptune and Triton. *Science*, *246*(4936), 1459–1466. https://doi.org/10.1126/science.246.4936.1459

Cao, X., & Paty, C. (2017). Diurnal and seasonal variability of Uranus's magnetosphere. *Journal of Geophysical Research: Space Physics*, *122*(6), 6318–6331. https://doi.org/10.1002/2017JA024063

Cao, X., & Paty, C. (2021). Asymmetric structure of Uranus' magnetopause controlled by IMF and planetary rotation. *Geophysical Research Letters*, *48*(4). https://doi.org/10.1029/2020GL091273

Coates, A. J., Crary, F. J., Young, D. T., Szego, K., Arridge, C. S., Bebesi, Z., et al. (2007). Ionospheric electrons in Titan's tail: Plasma structure during the Cassini T9 encounter. *Geophysical Research Letters*, *34*(24), L24S05. https://doi.org/10.1029/2007GL030919

Cochrane, C. J., Vance, S. D., Nordheim, T. A., Styczinski, M., Masters, A., & Regoli, L. H. (2021). In search of subsurface oceans within the Uranian moons (ArXiv ID:2105.06087). Retrieved from arxiv.org/abs/2105.06087

Connerney, J. E. P., Acuña, M. H., & Ness, N. F. (1991). The magnetic field of Neptune. *Journal of Geophysical Research*, *96*(S01), 19023. https://doi.org/10.1029/91ja01165

Cruikshank, D. P., Hamilton Brown, R., & Clark, R. N. (1984). Nitrogen on Triton. *Icarus*, *58*(2), 293–305. https://doi.org/10.1016/0019-1035(84)90046-0

Curtis, S. A., & Ness, N. F. (1986). Magnetostrophic balance in planetary dynamos: Predictions for Neptune's magnetosphere. *Journal of Geophysical Research*, *91*(A10), 11003. https://doi.org/10.1029/ja091ia10p11003

Dartnell, L. R., Nordheim, T. A., Patel, M. R., Mason, J. P., Coates, A. J., & Jones, G. H. (2015). Constraints on a potential aerial biosphere on Venus: I. Cosmic rays. *Icarus*, *257*, 396–405. https://doi.org/10.1016/j.icarus.2015.05.006

de la Haye, V., Waite, J., Jr, Cravens, T., Robertson, I., & Lebonnois, S. (2008). Coupled ion and neutral rotating model of Titan's upper atmosphere. *Icarus*, *197*(1), 110–136. https://doi.org/10.1016/j.icarus.2008.03.022

Decker, R. B., & Cheng, A. F. (1994). A model of Triton's role in Neptune's magnetosphere. *Journal of Geophysical Research*, *99*(E9), 19027. https://doi.org/10.1029/94JE01867

Delamere, P. A. (2009). Hybrid code simulations of the solar wind interaction with Pluto. *Journal of Geophysical Research: Space Physics*, *114*(A3). https://doi.org/10.1029/2008ja013756

Delitsky, M., & Thompson, W. (1987). Chemical processes in Triton's atmosphere and surface. *Icarus*, *70*(2), 354–365. https://doi.org/10.1016/0019-1035(87)90141-2

Desorgher, L., Fluckiger, E. O., Gurtner, M., Moser, M. R., & Butikofer, R. (2005). 11ATMOCOSMICS: A Geant 4 code for computing the interaction of cosmic rays with the Earth's atmosphere. *International Journal of Modern Physics A*, *20*(29), 6802–6804. https://doi.org/10.1142/S0217751X05030132

DiBraccio, G. A., & Gershman, D. J. (2019). Voyager 2 constraints on plasmoid-based transport at Uranus. *Geophysical Research Letters*, *46*(19), 10710–10718. https://doi.org/10.1029/2019GL083909

Exner, W., Heyner, D., Liuzzo, L., Motschmann, U., Shiota, D., Kusano, K., & Shibayama, T. (2018). Coronal mass ejection hits mercury: A.I.K.E.F. hybrid-code results compared to MESSENGER data. *Planetary and Space Science*, *153*, 89–99. https://doi.org/10.1016/j.pss.2017.12.016

Fatemi, S., Holmstrm, M., & Futaana, Y. (2012). The effects of lunar surface plasma absorption and solar wind temperature anisotropies on the solar wind proton velocity space distributions in the low-altitude lunar plasma wake. *Journal of Geophysical Research: Space Physics*, *117*(10), 1–13. https://doi.org/10.1029/2011JA017353

Fatemi, S., Poppe, A. R., Khurana, K. K., Holmström, M., & Delory, G. T. (2016). On the formation of Ganymede's surface brightness asymmetries: Kinetic simulations of Ganymede's magnetosphere. *Geophysical Research Letters*, *43*(10), 4745–4754. https://doi.org/10.1002/2016GL068363

Feyerabend, M., Liuzzo, L., Simon, S., & Motschmann, U. (2017). A three-dimensional model of Pluto's interaction with the solar wind during the new horizons encounter. *Journal of Geophysical Research: Space Physics*, *122*(10), 10356–10368. https://doi.org/10.1002/2017JA024456

Feyerabend, M., Simon, S., Motschmann, U., & Liuzzo, L. (2015). Filamented ion tail structures at Titan: A hybrid simulation study. *Planetary and Space Science*, *117*, 362–376. https://doi.org/10.1016/j.pss.2015.07.008

Gronoff, G., Lilensten, J., Desorgher, L., & Flückiger, E. (2009). Ionization processes in the atmosphere of Titan. *Astronomy & Astrophysics*, *506*(2), 955–964. https://doi.org/10.1051/0004-6361/200912371

Gronoff, G., Mertens, C., Lilensten, J., Desorgher, L., Flückiger, E., & Velinov, P. (2011). Ionization processes in the atmosphere of Titan. *Astronomy & Astrophysics*, *529*, A143. https://doi.org/10.1051/0004-6361/201015675

Gronoff, G., Norman, R. B., & Mertens, C. J. (2015). Computation of cosmic ray ionization and dose at Mars. I: A comparison of HZETRN and Planetocosmics for proton and alpha particles. *Advances in Space Research*, *55*(7), 1799–1805. https://doi.org/10.1016/j.asr.2015.01.028

Gurtner, M., Desorgher, L., Flückiger, E., & Moser, M. (2005). Simulation of the interaction of space radiation with the Martian atmosphere and surface. *Advances in Space Research*, *36*(11), 2176–2181. https://doi.org/10.1016/j.asr.2005.05.120

Gurtner, M., Desorgher, L., Flückiger, E., & Moser, M. (2006). A Geant4 application to simulate the interaction of space radiation with the Mercurian environment. *Advances in Space Research*, *37*(9), 1759–1763. https://doi.org/10.1016/j.asr.2004.12.015

Halekas, J. S., Bale, S. D., Mitchell, D. L., & Lin, R. P. (2005). Electrons and magnetic fields in the lunar plasma wake. *Journal of Geophysical Research*, *110*(A7). https://doi.org/10.1029/2004JA010991

Harris, C. D. K., Jia, X., Slavin, J. A., Toth, G., Huang, Z., & Rubin, M. (2021). Multi-Fluid MHD simulations of Europa's plasma interaction under different magnetospheric conditions. *Journal of Geophysical Research: Space Physics*, *126*(5), 1–24. https://doi.org/10.1029/2020ja028888

Hartkorn, O., & Saur, J. (2017). Induction signals from Callisto's ionosphere and their implications on a possible subsurface ocean. *Journal of Geophysical Research: Space Physics*, *122*(11), 11677–11697. https://doi.org/10.1002/2017JA024269

Holmström, M., Fatemi, S., Futaana, Y., & Nilsson, H. (2012). The interaction between the Moon and the solar wind. *Earth Planets and Space*, *264*(2), 237–245. https://doi.org/10.5047/eps.2011.06.040

Jellison, R., Macintyre, S., & Millero, F. J. (1999). Density and conductivity properties of Na-CO3-Cl-SO4 brine from Mono Lake, California, USA. *International Journal of Salt Lake Research*, *8*(1), 41–53. https://doi.org/10.1007/BF02442136

Jia, X., Walker, R. J., Kivelson, M. G., Khurana, K. K., & Linker, J. A. (2008). Three-dimensional MHD simulations of Ganymede's magnetosphere. *Journal of Geophysical Research*, *113*(6). https://doi.org/10.1029/2007JA012748

Jia, X., Walker, R. J., Kivelson, M. G., Khurana, K. K., & Linker, J. A. (2009). Properties of Ganymede's magnetosphere inferred from improved three-dimensional MHD simulations. *Journal of Geophysical Research*, *114*(9). https://doi.org/10.1029/2009JA014375

Kallio, E., & Janhunen, P. (2001). Atmospheric effects of proton precipitation in the Matrian atmosphere and its connection to the Mars-solar wind interaction. *Journal of Geophysical Research*, *106*(A4), 5617–5634. https://doi.org/10.1029/2000ja000239

Kallio, E., & Janhunen, P. (2003). Modelling the solar wind interaction with Mercury by a quasi-neutral hybrid model. *Annales Geophysicae*, *21*(11), 2133–2145. https://doi.org/10.5194/angeo-21-2133-2003

Kallio, E., Jarvinen, R., & Janhunen, P. (2006). Venus-solar wind interaction: Asymmetries in the escape of O$^+$ ions. *Planetary and Space Science*, *54*, 1472–1481. https://doi.org/10.1016/j.pss.2006.04.030

Kallio, E., Sillanpää, I., Jarvinen, R., Janhunen, P., Dougherty, M., Bertucci, C., & Neubauer, F. (2007). Morphology of the magnetic field near Titan: Hybrid model study of the Cassini T9 flyby. *Geophysical Research Letters*, *34*(24), L24S09. https://doi.org/10.1029/2007GL030827

Khurana, K. K., Fatemi, S., Lindkvist, J., Roussos, E., Krupp, N., Holmström, M., et al. (2017). The role of plasma slowdown in the generation of Rhea's Alfvén wings. *Journal of Geophysical Research: Space Physics*, *122*(2), 1778–1788. https://doi.org/10.1002/2016JA023595

Kimura, J., Nakagawa, T., & Kurita, K. (2009). Size and compositional constraints of Ganymede's metallic core for driving an active dynamo. *Icarus*, *202*(1), 216–224. https://doi.org/10.1016/j.icarus.2009.02.026

Kivelson, M., Bagenal, F., Kurth, W., Neubauer, F., Paranicas, C., & Saur, J. (2004). Magnetospheric interactions with satellites. In: *Jupiter: The planet, satellites and magnetosphere, m* (pp. 513–536).

Kivelson, M., Khurana, K., Stevenson, D., Bennett, L., Joy, S., Russell, C., et al. (1999). Europa and Callisto: Induced or intrinsic fields in a periodically varying plasma environment. *Journal of Geophysical Research*, *104*, 4609–4625. https://doi.org/10.1029/1998JA900095

Kivelson, M., Khurana, K. K., Russell, C. T., Volwerk, M., Walker, R. J., & Zimmer, C. (2000). Galileo magnetometer measurements: A stronger case for a subsurface ocean at Europa. *Science*, *289*(5483), 1340–1343. https://doi.org/10.1126/science.289.5483.1340

Kotova, A., Roussos, E., Krupp, N., & Dandouras, I. (2015). Modeling of the energetic ion observations in the vicinity of Rhea and Dione. *Icarus*, *258*, 402–417. https://doi.org/10.1016/j.icarus.2015.06.031

Krasnopolsky, V. A., & Cruikshank, D. P. (1995). Photochemistry of Triton's atmosphere and ionosphere. *Journal of geophysical research*, *100*(E10), 21271–21286. https://doi.org/10.1029/95JE01904

Krasnopolsky, V. A., Sandel, B. R., & Herbert, F. (1992). Properties of haze in the atmosphere of Triton. *Journal of Geophysical Research*, *97*(E7), 11695. https://doi.org/10.1029/92je00945

Kriegel, H., Simon, S., Meier, P., Motschmann, U., Saur, J., Wennmacher, A., et al. (2014). Ion densities and magnetic signatures of dust pick-up at Enceladus. *Journal of Geophysical Research*, *119*(4), 2740–2774. https://doi.org/10.1002/2013JA019440

Kriegel, H., Simon, S., Motschmann, U., Saur, J., Neubauer, F. M., Persoon, A. M., et al. (2011). Influence of negatively charged plume grains on the structure of Enceladus' Alfvén wings: Hybrid simulations versus Cassini Magnetometer data. *Journal of Geophysical Research*, *116*(10), 1–19. https://doi.org/10.1029/2011JA016842

Kriegel, H., Simon, S., Müller, J., Motschmann, U., Saur, J., Glassmeier, K.-H., & Dougherty, M. K. (2009). The plasma interaction of Enceladus: 3D hybrid simulations and comparison with Cassini MAG data. *Planetary and Space Science*, *57*(14–15), 2113–2122. https://doi.org/10.1016/j.pss.2009.09.025

Krimigis, S. M., Armstrong, T. P., Axford, W. I., Bostrom, C. O., Cheng, A. F., Gloeckler, G., et al. (1989). Hot plasma and energetic particles in Neptune's magnetosphere. *Science*, *246*(4936), 1483–1489. https://doi.org/10.1126/science.246.4936.1483

Krupp, N., Kotova, A., Roussos, E., Simon, S., Liuzzo, L., Paranicas, C., et al. (2020). Magnetospheric interactions of Saturn's Moon Dione (2005–2015). *Journal of Geophysical Research: Space Physics*, *125*(6). https://doi.org/10.1029/2019JA027688

Ledvina, S. A., Brecht, S. H., & Cravens, T. E. (2012). The orientation of Titan's dayside ionosphere and its effects on Titan's plasma interaction. *Earth Planets and Space*, *64*, 207–230. https://doi.org/10.5047/eps.2011.08.009

Lellouch, E., Blanc, M., Oukbir, J., & Longaretti, P. Y. (1992). A model of Triton's atmosphere and ionosphere. *Advances in Space Research*, *12*(11), 113–121. https://doi.org/10.1016/0273-1177(92)90427-Y

Lindkvist, J., Holmström, M., Khurana, K. K., Fatemi, S., & Barabash, S. (2015). Callisto plasma interactions: Hybrid modeling including induction by a subsurface ocean. *Journal of Geophysical Research: Space Physics*, *120*, 4877–4889. https://doi.org/10.1002/2015ja021212

Lipatov, A., & Combi, M. (2006). Effects of kinetic processes in shaping Io's global plasma environment: A 3D hybrid model. *Icarus*, *180*, 412–427. https://doi.org/10.1016/j.icarus.2005.08.012

Lipatov, A., Cooper, J., Paterson, W., Sittler, E., Hartle, R., & Simpson, D. (2010). Jovian plasma torus interaction with Europa: 3D hybrid kinetic simulation. First results. *Planetary and Space Science*, *58*(13), 1681–1691. https://doi.org/10.1016/j.pss.2010.06.015

Lipatov, A., Cooper, J., Paterson, W., Sittler, E., Jr, Hartle, R., & Simpson, D. (2013). Jovian plasma torus interaction with Europa. Plasma wake structure and effect of inductive magnetic field: 3D hybrid kinetic simulation. *Planetary and Space Science*, *77*, 12–24. https://doi.org/10.1016/j.pss.2013.01.009

Lipatov, A., Sittler, E., Hartle, R., Cooper, J., & Simpson, D. (2012). Saturn's magnetosphere interaction with Titan for T9 encounter: 3D hybrid modeling and comparison with CAPS observations. *Planetary and Space Science*, *61*(1), 66–78. https://doi.org/10.1016/j.pss.2011.08.017

Liuzzo, L., Feyerabend, M., Simon, S., & Motschmann, U. (2015). The impact of Callisto's atmosphere on its plasma interaction with the Jovian magnetosphere. *Journal of Geophysical Research - A: Space Physics*, *120*(11), 9401–9427. https://doi.org/10.1002/2015JA021792

Liuzzo, L., Poppe, A. R., Halekas, J. S., Simon, S., & Cao, X. (2021). Investigating the Moon's interaction with the terrestrial magnetotail lobe plasma. *Geophysical Research Letters*, *48*(9), 1–11. https://doi.org/10.1029/2021GL093566

Liuzzo, L., Poppe, A. R., Paranicas, C., Nénon, Q., Fatemi, S., & Simon, S. (2020). Variability in the energetic electron bombardment of Ganymede. *Journal of Geophysical Research: Space Physics*, *9*, 1–35. https://doi.org/10.1029/2020JA028347

Liuzzo, L., Simon, S., & Feyerabend, M. (2018). Observability of Callisto's inductive signature during the JUpiter ICy Moons Explorer mission. *Journal of Geophysical Research: Space Physics*, *123*(11), 9045–9054. https://doi.org/10.1029/2018JA025951

Liuzzo, L., Simon, S., Feyerabend, M., & Motschmann, U. (2016). Disentangling plasma interaction and induction signatures at Callisto: The Galileo C10 flyby. *Journal of Geophysical Research: Space Physics*, *121*(9), 8677–8694. https://doi.org/10.1002/2016JA023236

Liuzzo, L., Simon, S., Feyerabend, M., & Motschmann, U. (2017). Magnetic signatures of plasma interaction and induction at Callisto: The Galileo C21, C22, C23, and C30 flybys. *Journal of Geophysical Research: Space Physics*, *122*(7), 7364–7386. https://doi.org/10.1002/2017JA024303

Liuzzo, L., Simon, S., & Regoli, L. (2019a). Energetic electron dynamics near Callisto. *Planetary and Space Science*, *179*(August), 104726. https://doi.org/10.1016/j.pss.2019.104726

Liuzzo, L., Simon, S., & Regoli, L. (2019b). Energetic ion dynamics near Callisto. *Planetary and Space Science*, *166*, 23–53. https://doi.org/10.1016/j.pss.2018.07.014

Luspay-Kuti, A., Mandt, K., Jessup, K. L., Kammer, J., Hue, V., Hamel, M., & Filwett, R. (2017). Photochemistry on Pluto - I. Hydrocarbons and aerosols. *Monthly Notices of the Royal Astronomical Society*, *472*(1), 104–117. https://doi.org/10.1093/mnras/stx1362

Luspay-Kuti, A., Mandt, K. E., Plessis, S., & Greathouse, T. K. (2015). Effects of nitrogen photoabsorption cross section resolution on minor species vertical profiles in titan's upper atmosphere. *The Astrophysical Journal Letters*, *801*(1), L14. https://doi.org/10.1088/2041-8205/801/1/L14

Luspay-Kuti, A., Mandt, K. E., Westlake, J. H., Plessis, S., & Greathouse, T. K. (2016). The role of nitrogen in Titan's upper atmospheric hydrocarbon chemistry over the solar cycle. *The Astrophysical Journal*, *823*(2), 163. https://doi.org/10.3847/0004-637X/823/2/163

Mandt, K. E., Gell, D. A., Perry, M., Hunter Waite, J., Crary, F. A., Young, D., et al. (2012). Ion densities and composition of Titan's upper atmosphere derived from the Cassini Ion Neutral Mass Spectrometer: Analysis methods and comparison of measured ion densities to photochemical model simulations. *Journal of Geophysical Research*, *117*(E10). https://doi.org/10.1029/2012JE004139

Mandt, K. E., Luspay-Kuti, A., Hamel, M., Jessup, K. L., Hue, V., Kammer, J., & Filwett, R. (2017). Photochemistry on Pluto: Part II HCN and nitrogen isotope fractionation. *Monthly Notices of the Royal Astronomical Society*, *472*(1), 118–128. https://doi.org/10.1093/MNRAS/STX1587

Marion, G., Kargel, J., Catling, D., & Lunine, J. (2012). Modeling ammonia–ammonium aqueous chemistries in the Solar System's icy bodies. *Icarus*, *220*(2), 932–946. https://doi.org/10.1016/j.icarus.2012.06.016

Martinecz, C., Boesswetter, A., Fränz, M., Roussos, E., Woch, J., Krupp, N., et al. (2009). Plasma environment of Venus: Comparison of Venus Express ASPERA-4 measurements with 3-D hybrid simulations. *Journal of Geophysical Research*, *114*, E00B30. https://doi.org/10.1029/2008JE003174

Mauk, B. H., Keath, E. P., Kane, M., Krimigis, S. M., Cheng, A. F., Acuña, M. H., et al. (1991). The magnetosphere of Neptune: Hot plasmas and energetic particles. *Journal of Geophysical Research*, *96*(S01), 19061. https://doi.org/10.1029/91JA01820

McKinnon, W. B., & Kirk, R. L. (2007). Triton. In *Encyclopedia of the solar system* (pp. 483–502). Elsevier. https://doi.org/10.1016/B978-012088589-3/50030-X

Mejnertsen, L., Eastwood, J. P., Chittenden, J. P., & Masters, A. (2016). Global MHD simulations of Neptune's magnetosphere. *Journal of Geophysical Research: Space Physics*, *121*(8), 7497–7513. https://doi.org/10.1002/2015ja022272

Modolo, R., Chanteur, G. M., Wahlund, J.-E., Canu, P., Kurth, W. S., Gurnett, D., & Bertucci, C. (2007). Plasma environment in the wake of Titan from hybrid simulation: A case study. *Geophysical Research Letters*, *34*, 10. https://doi.org/10.1029/2007gl030489

Modolo, R., & Chanteur, G. M. M. (2008). A global hybrid model for Titan's interaction with the Kronian plasma: Application to the Cassini Ta flyby. *Journal of Geophysical Research: Space Physics*, *113*(A1). https://doi.org/10.1029/2007ja012453

Modolo, R., Hess, S., Mancini, M., Leblanc, F., Chaufray, J.-Y., Brain, D., et al. (2016). Mars-solar wind interaction: LatHyS, an improved parallel 3-D multispecies hybrid model. *Journal of Geophysical Research: Space Physics*, *121*(7), 6378–6399. https://doi.org/10.1002/2015JA022324

Modolo, R., Wahlund, J.-E., Boström, R., Canu, P., Kurth, W. S., Gurnett, D., et al. (2007). Far plasma wake of Titan from the RPWS observations: A case study. *Geophysical Research Letters*, *34*, L24S04. https://doi.org/10.1029/2007gl030482

Müller, J., Simon, S., Motschmann, U., Schüle, J., Glassmeier, K. H., & Pringle, G. J. (2011). A.I.K.E.F.: Adaptive hybrid model for space plasma simulations. *Computer Physics Communications*, *182*(4), 946–966. https://doi.org/10.1016/j.cpc.2010.12.033

Ness, N., Acuña, M., Burlaga, L., Connerney, J., Lepping, R., & Neubauer, F. (1989). Magnetic fields at Neptune. *Science*, *246*(4936), 1473–1478. https://doi.org/10.1126/science.246.4936.1473

Ness, N., Acuña, M., & Connerney, J. (1995). Neptune's magnetic field and field-geometric properties. In D. Cruikshank (Ed.), *Neptune and triton* (pp. 141–168). University of Arizona Press.

Neubauer, F. (1980). Nonlinear standing Alfvén wave current system at Io: Theory. *Journal of Geophysical Research*, *85*(9), 1171–1178. https://doi.org/10.1029/JA085iA03p01171

Neubauer, F. (1998). The sub-Alfvenic interaction of the Galilean satellites with the Jovian magnetosphere. *Journal of Geophysical Research*, *103*, 843–19866. https://doi.org/10.1029/97JE03370

Neubauer, F. (1999). Alfvén wings and electromagnetic induction in the interiors: Europa and Callisto. *Journal of Geophysical Research*, *104*, 28671–28684. https://doi.org/10.1029/1999JA900217

Neubauer, F., Backes, H., Dougherty, M. K., Wennmacher, A., Russell, C. T., Coates, A., et al. (2006). Titan's near magnetotail from magnetic field and plasma observations and modelling: Cassini flybys TA, TB and T3. *Journal of Geophysical Research*, *111*, A10220. https://doi.org/10.1029/2006ja011676

Nimmo, F., & Spencer, J. (2015). Powering Triton's recent geological activity by obliquity tides: Implications for Pluto geology. *Icarus*, *246*, 2–10. https://doi.org/10.1016/j.icarus.2014.01.044

Nordheim, T., Dartnell, L., Desorgher, L., Coates, A., & Jones, G. (2015). Ionization of the Venusian atmosphere from solar and galactic cosmic rays. *Icarus*, *245*, 80–86. https://doi.org/10.1016/j.icarus.2014.09.032

Nordheim, T., Hand, K. P., & Paranicas, C. (2018). Preservation of potential biosignatures in the shallow subsurface of Europa. *Nature Astronomy*, *2*(8), 673–679. https://doi.org/10.1038/s41550-018-0499-8

Nordheim, T., Jasinski, J., & Hand, K. (2019). Galactic cosmic-ray bombardment of Europa's surface. *The Astrophysical Journal*, *881*(2), L29. https://doi.org/10.3847/2041-8213/ab3661

Ohno, K., Zhang, X., Tazaki, R., & Okuzumi, S. (2021). Haze formation on Triton. *The Astrophysical Journal*, *912*(1), 37. https://doi.org/10.3847/1538-4357/abee82

Paty, C., & Winglee, R. (2004). Multi-fluid simulations of Ganymede's magnetosphere. *Geophysical Research Letters*, *31*(24), 1–5. https://doi.org/10.1029/2004GL021220

Paty, C., & Winglee, R. (2006). The role of ion cyclotron motion at Ganymede: Magnetic field morphology and magnetospheric dynamics. *Geophysical Research Letters*, *33*(10). https://doi.org/10.1029/2005GL025273

Perkins, S., Cullen, D., & Seltzer, S. (1991). *Tables and graphs of electron-interaction cross sections from 10 eV to 100 GeV derived from the LLNL evaluated electron data library (EEDL), Z = 1–100* (Technical Report, UCRL-50400 Vol. *31*). Livermore, CA: Lawrence Livermore National Laboratory (LLNL). https://doi.org/10.2172/5691165

Poppe, A. R., Fatemi, S., Halekas, J. S., Holmström, M., & Delory, G. T. (2014). ARTEMIS observations of extreme diamagnetic fields in the lunar wake. *Geophysical Research Letters*, *41*(11), 3766–3773. https://doi.org/10.1002/2014GL060280

Poppe, A. R., Fatemi, S., & Khurana, K. K. (2018). Thermal and energetic ion dynamics in Ganymede's magnetosphere. *Journal of Geophysical Research: Space Physics*, *123*(6), 4614–4637. https://doi.org/10.1029/2018JA025312

Raponi, A., De Sanctis, M., Carrozzo, F., Ciarniello, M., Castillo-Rogez, J., Ammannito, E., et al. (2019). Mineralogy of Occator crater on Ceres and insight into its evolution from the properties of carbonates, phyllosilicates, and chlorides. *Icarus*, *20*, 83–96. https://doi.org/10.1016/j.icarus.2018.02.001

Regoli, L. H., Roussos, E., Feyerabend, M., Jones, G. H., Krupp, N., Coates, A. J., et al. (2016). Access of energetic particles to Titan's exobase: A study of Cassini's T9 flyby. *Planetary and Space Science*, *130*, 40–53. https://doi.org/10.1016/j.pss.2015.11.013

Richards, P. G., Woods, T. N., & Peterson, W. K. (2006). HEUVAC: A new high resolution solar EUV proxy model. *Advances in Space Research*, *37*(2), 315–322. https://doi.org/10.1016/j.asr.2005.06.031

Richardson, J. D. (1993). A quantitative model of plasma in Neptune's magnetosphere. *Geophysical Research Letters*, *20*(14), 1467–1470. https://doi.org/10.1029/93GL01353

Richardson, J. D., Eviatar, A., & Delitsky, M. L. (1990). The Triton torus revisited. *Geophysical Research Letters*, *17*(10), 1673–1676. https://doi.org/10.1029/GL017i010p01673

Richardson, J. D., & McNutt, R. L. (1990). Low-energy plasma in Neptune's magnetosphere. *Geophysical Research Letters*, *17*(10), 1689–1692. https://doi.org/10.1029/GL017i010p01689

Roussos, E., Mueller, J., Simon, S., Boesswetter, A., Motschmann, U., Krupp, N., et al. (2008). Plasma and fields in the wake of Rhea: 3-D hybrid simulation and comparison with Cassini data. *Annales Geophysicae*, *26*(3), 619–637. https://doi.org/10.5194/angeo-26-619-2008

Saur, J., Duling, S., Roth, L., Jia, X., Strobel, D. F., Feldman, P. D., et al. (2015). The search for a subsurface ocean in Ganymede with Hubble Space Telescope observations of its auroral ovals. *Journal of Geophysical Research: Space Physics*, *120*(3), 1715–1737. https://doi.org/10.1002/2014JA020778

Saur, J., Grambusch, T., Duling, S., Neubauer, F. M., & Simon, S. (2013). Magnetic energy fluxes in sub-Alfvénic planet star and moon planet interactions. *Astronomy and Astrophysics*, *552*(A119), 1–20. https://doi.org/10.1051/0004-6361/201118179

Saur, J., Neubauer, F. M., & Glassmeier, K.-H. H. (2010). Induced magnetic fields in solar system bodies. *Space Science Reviews*, *152*(1–4), 391–421. https://doi.org/10.1007/s11214-009-9581-y

Saur, J., Neubauer, F. M., Strobel, D. F., & Summers, M. E. (1999). Three-dimensional plasma simulation of Io's interaction with the Io plasma torus: Asymmetric plasma flow. *Journal of Geophysical Research: Space Physics*, *104*(A11), 25105–25126. https://doi.org/10.1029/1999ja900304

Schilling, N., Khurana, K. K., & Kivelson, M. G. (2004). Limits on an intrinsic dipole moment in Europa. *Journal of Geophysical Research: Planets*, *109*(5), 1–10. https://doi.org/10.1029/2003JE002166

Schilling, N., Neubauer, F. M., & Saur, J. (2007). Time-varying interaction of Europa with the jovian magnetosphere: Constraints on the conductivity of Europa's subsurface ocean. *Icarus*, *192*(1), 41–55. https://doi.org/10.1016/j.icarus.2007.06.024

Schilling, N., Neubauer, F. M., & Saur, J. (2008). Influence of the internally induced magnetic field on the plasma interaction of Europa. *Journal of Geophysical Research*, *113*, A03203. https://doi.org/10.1029/2007JA012842

Seufert, M., Saur, J., & Neubauer, F. M. (2011). Multi-frequency electromagnetic sounding of the Galilean moons. *Icarus*, *214*(2), 477–494. https://doi.org/10.1016/j.icarus.2011.03.017

Shock, E. L., & McKinnon, W. B. (1993). Hydrothermal processing of cometary volatiles—Applications to Triton. *Icarus*, *106*(2), 464–477. https://doi.org/10.1006/icar.1993.1185

Sillanpää, I., & Johnson, R. E. (2015). The role of ion-neutral collisions in Titan's magnetospheric interaction. *Planetary and Space Science*, *108*, 73–86. https://doi.org/10.1016/j.pss.2015.01.007

Sillanpää, I., Kallio, E., Janhunen, P., Schmidt, W., Mursula, K., Vilppola, J., & Tanskanen, P. (2006). Hybrid simulation study of ion escape at Titan for different orbital positions. *Advances in Space Research*, *38*(4), 799–805. https://doi.org/10.1016/j.asr.2006.01.005

Simon, S. (2015). An analytical model of sub-Alfvénic moon-plasma interactions with application to the hemisphere coupling effect. *Journal of Geophysical Research: Space Physics*, *120*(9), 7209–7227. https://doi.org/10.1002/2015ja021529

Simon, S., Kriegel, H., Saur, J., Wennmacher, A., Neubauer, F. M., Roussos, E., & Dougherty, M. K. (2012). Analysis of Cassini magnetic field observations over the poles of Rhea. *Journal of Geophysical Research: Space Physics*, *117*(A7). https://doi.org/10.1029/2012ja017747

Simon, S., Liuzzo, L., & Addison, P. (2021). Role of the ionospheric conductance profile in sub-Alfvenic moon-magnetosphere interactions: An analytical model. *Journal of Geophysical Research*, *126*(7), 1–27. https://doi.org/10.1029/2021ja029191

Simon, S., & Motschmann, U. (2009). Titan's induced magnetosphere under non-ideal upstream conditions: 3D multi-species hybrid simulations. *Planetary and Space Science*, *57*(14–15), 2001–2015. https://doi.org/10.1016/j.pss.2009.08.010

Simon, S., Saur, J., Neubauer, F. M., Motschmann, U., & Dougherty, M. K. (2009). Plasma wake of Tethys: Hybrid simulations versus Cassini MAG data. *Geophysical Research Letters*, *36*(4), L04108. https://doi.org/10.1029/2008GL036943

Simon, S., Saur, J., Neubauer, F. M., Wennmacher, A., & Dougherty, M. K. (2011). Magnetic signatures of a tenuous atmosphere at Dione. *Geophysical Research Letters*, *38*(15), L15102. https://doi.org/10.1029/2011GL048454

Simon, S., Wennmacher, A., Neubauer, F. M., Bertucci, C., Kriegel, H., Saur, J., et al. (2010). Titan's highly dynamic magnetic environment: A systematic survey of Cassini magnetometer observations from flybys TA–T62. *Planetary and Space Science*, *58*(10), 1230–1251. https://doi.org/10.1016/j.pss.2010.04.021

Sittler, E., Cooper, J., Hartle, R., Paterson, W., Christian, E., Lipatov, A., et al. (2013). Plasma ion composition measurements for Europa. *Planetary and Space Science*, *88*, 26–41. https://doi.org/10.1016/j.pss.2013.01.013

Sittler, E., & Hartle, R. (1996). Triton's ionospheric source: Electron precipitation or photoionization. *Journal of Geophysical Research: Space Physics*, *101*(A5), 10863–10876. https://doi.org/10.1029/96JA00398

Sittler, E., Hartle, R., Johnson, R., Cooper, J., Lipatov, A., Bertucci, C., et al. (2010). Saturn's magnetospheric interaction with Titan as defined by Cassini encounters T9 and T18: New results. *Planetary and Space Science*, *58*(3), 327–350. https://doi.org/10.1016/j.pss.2009.09.017

Smith, B. A., Soderblom, L. A., Banfield, D., Basilevsky, A., Beebe, R., Bollinger, K., et al. (1989). Voyager 2 at Neptune: Imaging science results. *Science*, *246*(4936), 1422–1449. https://doi.org/10.1126/science.246.4936.1422

Strobel, D. F., Cheng, A. F., Summers, M. E., & Strickland, D. J. (1990). Magnetospheric interaction with Triton's ionosphere. *Geophysical Research Letters*, *917*(10), 1661–1664. https://doi.org/10.1029/gl017i010p01661

Strobel, D. F., Saur, J., Feldman, P. D., & McGrath, M. A. (2002). Hubble Space Telescope space telescope imaging spectrograph search for an atmosphere on Callisto: A Jovian unipolar inductor. *The Astrophysical Journal*, *581*(1), 51–54. https://doi.org/10.1086/345803

Strobel, D. F., & Zhu, X. (2017). Comparative planetary nitrogen atmospheres: Density and thermal structures of Pluto and Triton. *Icarus*, *291*, 55–64. https://doi.org/10.1016/j.icarus.2017.03.013

Styczinski, M. J., & Harnett, E. M. (2021). Induced magnetic moments from a nearly spherical ocean. *Icarus*, *354*, 114020. https://doi.org/10.1016/j.icarus.2020.114020

Summers, M. E., & Strobel, D. F. (1991). Triton's atmosphere: A source of N and H for Neptune's magnetosphere. *Geophysical Research Letters*, *18*(12), 2309–2312. https://doi.org/10.1029/91gl01334

Szego, K., Bebesi, Z., Bertucci, C., Coates, A. J., Crary, F., Erdos, G., et al. (2007). Charged particle environment of Titan during the T9 flyby. *Geophysical Research Letters*, *34*(24), L24S03. https://doi.org/10.1029/2007GL030677

Thompson, W., & Sagan, C. (1990). Color and chemistry on Triton. *Science*, *250*(4979), 415–418. https://doi.org/10.1126/science.11538073

Trafton, L. (1984). Large seasonal variations in Triton's atmosphere. *Icarus*, *58*(2), 312–324. https://doi.org/10.1016/0019-1035(84)90048-4

Travnicek, P., Hellinger, P., Schriver, D., Bale, S. D., Trávníček, P., Hellinger, P., & Bale, S. D. (2005). Structure of the lunar wake: Two-dimensional global hybrid simulations. *Geophysical Research Letters*, *32*(6), L06102. https://doi.org/10.1029/2004GL022243

Usoskin, I. G., Desorgher, L., Velinov, P., Storini, M., Flückiger, E. O., Bütikofer, R., & Kovaltsov, G. A. (2009). 3Ionization of the earth's atmosphere by solar and galactic cosmic rays. *Acta Geophysica*, *57*(1), 88–101. https://doi.org/10.2478/s11600-008-0019-9

Vance, S. D., Styczinski, M. J., Bills, B. G., Cochrane, C. J., Soderlund, K. M., Gómez-Pérez, N., & Paty, C. (2021). Magnetic induction responses of Jupiter's Ocean Moons including effects from adiabatic convection. *Journal of Geophysical Research: Planets*, *126*(2), 1–25. https://doi.org/10.1029/2020JE006418

Vernisse, Y., Kriegel, H., Wiehle, S., Motschmann, U., & Glassmeier, K. H. (2013). Stellar winds and planetary bodies simulations: Lunar type interaction in super-Alfvénic and sub-Alfvénic flows. *Planetary and Space Science*, *84*, 37–47. https://doi.org/10.1016/j.pss.2013.04.004

Wiehle, S., Plaschke, F., Motschmann, U., Glassmeier, K. H., Auster, H. U., Angelopoulos, V., et al. (2011). First lunar wake passage of ARTEMIS: Discrimination of wake effects and solar wind fluctuations by 3D hybrid simulations. *Planetary and Space Science*, *59*(8), 661–671. https://doi.org/10.1016/j.pss.2011.01.012

Wong, M. L., Fan, S., Gao, P., Liang, M. C., Shia, R. L., Yung, Y. L., et al. (2017). The photochemistry of Pluto's atmosphere as illuminated by New Horizons. *Icarus*, *287*, 110–115. https://doi.org/10.1016/j.icarus.2016.09.028

Zhang, M., Richardson, J. D., & Sittler, E. C. (1991). Voyager 2 electron observations in the magnetosphere of Neptune. *Journal of Geophysical Research*, *96*(S01), 19085. https://doi.org/10.1029/91JA01857

Zimmer, C., Khurana, K. K., & Kivelson, M. G. (2000). Subsurface Oceans on Europa and Callisto: Constraints from Galileo magnetometer observations. *Icarus*, *347*(2), 329–347. https://doi.org/10.1006/icar.2000.6456